Nucleic Acids Research, 2025, **53**, gkaf294
https://doi.org/10.1093/nar/gkaf294
RNA and RNA-protein complexes

Chromatin-associated α-satellite RNA maintains chromosome stability by reestablishing SAF-A in the mitotic cell cycle

Bingbing Ren[1,2,*,†], Yinchun Zhong[3,†], Yan Yang[3,†], Shuhui Chang[4], Yalun Li[1], Mengzhen You[1], Ge Shan[1,3], Xueren Wang[5,6,*], Enguo Chen[1,*]

[1]Department of Pulmonary and Critical Care Medicine, Regional Medical Center for National Institute of Respiratory Disease, Sir Run Run Shaw Hospital, School of Medicine, Zhejiang University, Hangzhou 310016, China
[2]Central Lab of Biomedical Research Center, Sir Run Run Shaw Hospital, School of Medicine, Zhejiang University, Hangzhou 310020, China
[3]Department of Clinical Laboratory, The First Affiliated Hospital of USTC, Division of Life Science and Medicine, University of Science and Technology of China, Hefei 230027, China
[4]Department of General Surgery, Sir Run Run Shaw Hospital, Zhejiang University, Hangzhou 310016, China
[5]Department of Anesthesiology, Shanxi Bethune Hospital, Taiyuan 030032, China.
[6]Department of Anesthesiology, Tongji Hospital, Tongji Medical College, Huazhong University of Science and Technology, Wuhan 430030, China

[*]To whom correspondence should be addressed. Tel: +86 17857001826; Email: renbb@zju.edu.cn
Correspondence may also be addressed to Enguo Chen. Email: 3195024@zju.edu.cn
Correspondence may also be addressed to Xueren Wang. Email: xrwang@hust.edu.cn
[†]The first three authors should be regarded as Joint First Authors.

Abstract

α-Satellite is the largest class of tandem repeats and is located on all human chromosome centromeres. Non-coding α-satellite RNAs have been observed in various cell types and are known to play crucial roles in maintaining genome stability. In this study, we demonstrated that α-satellite RNAs are dynamically expressed, heterogeneous transcripts that are regulated by Aurora kinases and closely associated with centromere chromatin throughout the mitotic cell cycle. We identified scaffold attachment factor A (SAF-A) as a previously uncharacterized α-satellite RNA binding protein. Depletion of either α-satellite RNA or SAF-A resulted in chromosome missegregation, revealing that their concerted action is essential for preserving genome integrity during the mitotic cell cycle. Our result demonstrated that SAF-A is excluded from the chromatin genome-wide during mitosis, and α-satellite RNAs are required for the recruitment of SAF-A upon mitotic exit. Both α-satellite RNAs and SAF-A are essential in safeguarding the human genome against chromosomal instability during mitosis. Moreover, α-satellite RNAs and SAF-A aid in the reassembly of the nuclear lamina. Our results provide novel insights into the features, regulations, and functional roles of α-satellite RNAs and propose a model for the dismantling and reformation of the SAF-A nuclear scaffold during mitosis.

Received: July 6, 2024. **Revised:** March 21, 2025. **Editorial Decision:** March 24, 2025. **Accepted:** March 28, 2025

Graphical abstract

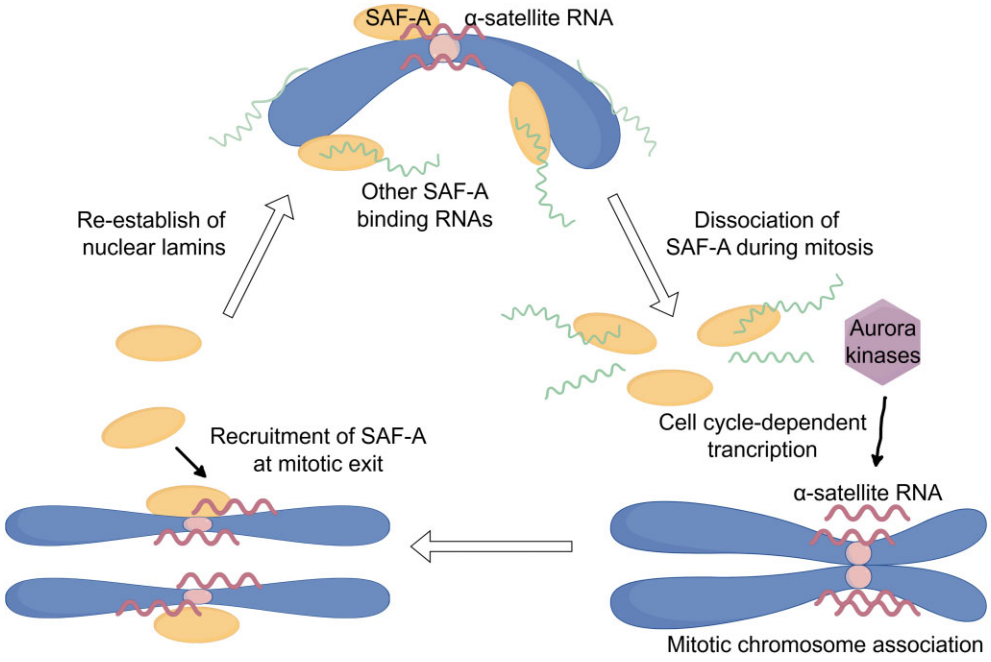

Introduction

Satellite DNA refers to the tandem repeat sequences that are usually located within the centromeric and pericentromeric regions of the genome [1]. Among the various types of human satellites, α-satellite repeats, which encompass all chromosome centromeres, form the largest class with a total length of approximately 85.2 Mb and represent approximately 2.8% of the human genome (T2T-CHM13v2.0) [2, 3]. The ∼171 bp AT-rich monomers of α-satellites are usually organized into highly homogenous higher-order repeats [4].

α-Satellite RNAs, as the transcripts of the α-satellite repeats, were first identified in Hela cells and were primarily localized at the nucleolus before being directed to the centromere via CENP-C at the onset of mitosis [5]. A multitude of evidence has established that RNA polymerase II is the major RNA polymerase that is responsible for α-satellite RNA transcription [5–7]. The transcription of centromeric repeats is common across various eukaryotic species, despite differences in the satellite sequences [8]. In mice, the centromere contains two primary classes of repetitive sequences: minor and major satellite repeats. Minor satellite repeats consist of tandem arrays of 120-bp sequences that define the CENP-A-bounded core centromere, and major satellite repeats of 234-bp units located pericentrically, which create the heterochromatin that flanks the minor satellite repeats [1].

Subsequent studies have reported cell cycle-specific transcription of α-satellite RNAs in various cell types, where they colocalize with CENP-A and other centromere proteins [6, 9, 10]. Furthermore, α-satellite RNAs have been demonstrated to have specific functions in normal human cells, particularly within the centromere regions, where they participate in the recruitment of centromere proteins for kinetochore assembly or in the establishment and maintenance of heterochromatin [9–11]. The regulation of α-satellite RNA expression is critical, as both the overexpression and suppression of these RNAs have been demonstrated in response to stress and have been observed in numerous human cancers [12–15]. However, based on the findings from previous research, the size, localization, and regulators of α-satellite RNA remain unclear or inconsistent [16, 17]. α-Satellite RNA has been shown to interact with specific sets of RNA-binding proteins [17]. By forming complexes with centromere proteins CENP-A, CENP-B, and CENP-C, α-satellite RNA was shown to have essential roles in maintaining human centromere functionality [9–11]. Moreover, α-satellite RNA has been reported to interact with SUV39H1, which is the histone methyltransferase that is responsible for H3K9me3, thereby contributing to the maintenance of constitutive heterochromatin [18].

Scaffold attachment factor-A (SAF-A), also known as hnRNPU, is an abundant heterogeneous nuclear ribonucleoprotein (hnRNP) and was initially identified as the major nuclear scaffold component [19, 20]. SAF-A exhibits dual binding capabilities, interacting with both DNA and RNA through distinct binding domains. Specifically, it engages with RNA via the low complexity RGG domain and associates with AT-rich DNA regions via the SAP (SAF-A/B, Acinus, and PIAS) domain [19, 20]. Notably, α-satellite tandem repeats also have an AT-rich composition. In addition to its established roles in splicing regulation, several recent studies have suggested that SAF-A may play a fundamental and general role in the nuclear organization in interphase [21–24]. SAF-A depletion leads to the pronounced chromatin condensation of gene-rich regions and global changes in genome 3D architecture [22, 23]. Spatially, in most mammalian cells, centromeres are preferentially located at the nuclear periphery and tethered to the nuclear lamina through lamina-associated domains (LADs) [25, 26]. Nuclear membrane proteins, such as lamin-associated polypeptide 2 (LAP2), have been shown to directly interact with both lamins and chromosomes during nuclear lamina reassembly [27]. Research in mouse hepatocytes has shown that SAF-A depletion increases the coverage of LADs in the genome and leads to global chromatin condensation [22]. No-

ticeably, RNA components seem to be required for the localization of SAF-A on chromatin [23, 28]. A SAF-A/RNA mesh model has been proposed and supported, in which SAF-A forms a homogeneous mesh together with chromatin-associated RNAs (caRNAs) that regulate the high-order chromatin structure in interphase cells [21, 29]. As an evolutionarily conserved RNA-binding protein, SAF-A has been reported to interact with a wide variety of RNAs in different cell types [30, 31]. In particular, a recent study revealed that repetitive non-coding sequences of pre-mRNAs and lncRNAs can serve as scaffold RNAs to counter chromatin compaction and maintain the chromosome territory architecture together with SAF-A [23]. At present, most studies have demonstrated the role of SAF-A/RNA in regulating the interphase chromatin structure, and few have focused on the role of SAF-A/RNA in mitosis. A recent study showed that during mitosis, SAF-A, together with most of its interacting RNAs, needs to be evicted from the condensing chromosomes [32]. This raises the question of how the SAF-A/RNA scaffold is disassembled and rebuilt when the cell enters and exits mitosis.

In this study, we report the identification of SAF-A as a previously uncharacterized α-satellite RNA binding protein. Through various experiments and analyses, we demonstrate that α-satellite RNAs are dynamically expressed and remain associated with centromeric chromatin throughout the mitotic cell cycle. Specific interactions between α-satellite RNAs and SAF-A were investigated both *in vitro* and *in vivo*. We also demonstrated that the depletion of either α-satellite RNA or SAF-A resulted in chromosome missegregation phenotypes during mitosis. Furthermore, interference with α-satellite RNAs substantially influenced the chromatin relocalization of SAF-A and subsequently affected the nuclear lamina reassembly at the mitotic exit.

Materials and methods

Cell culture

The human and mouse cell lines used in this study were purchased from ATCC (http://www.atcc.org). Cells were cultured in DMEM medium with 10% fetal bovine serum and 1% penicillin/streptomycin under standard conditions of 37°C with 5% CO_2.

Transfection of siRNA and shRNA constructs

The shRNA plasmids were obtained from the MISSION shRNA library (Sigma-Aldrich, Germany). Transfections of the siRNA and shRNA plasmids were performed using Lipofectamine 2000 (Invitrogen) according to the manufacturer's instructions. Detailed information on the siRNAs and shRNA plasmids used in this study is provided in Supplementary Tables S1 and S2.

RNA extraction and RT-qPCR

RNA was extracted using TRIzol (Invitrogen) according to the manufacturer's instructions. To remove the DNA, the total extract was treated with DNase I (Thermo) and purified using phenol-chloroform extraction. The RNA concentration was measured with a Nanodrop 2000c (Thermo Fisher) before being reverse transcribed using the ABScript cDNA first-strand synthesis kit (ABclonal). Quantitative polymerase chain reaction (PCR) was performed with a 2 × Q3 SYBR qPCR master mix (ToloBio) on a CFX96 real-time PCR system (Bio-Rad) using standard procedures. Detailed information on the primers used in this study is provided in Supplementary Table S1.

Northern blot

For northern blot analysis, 0.2–5 μg of total RNA was separated on a 6% TBE-urea gel (1 × TBE, 6% acryl/bis, 5 M urea, 0.08% ammonium persulfate, and 0.1% TEMED) and transferred to an Amersham Hybond-N + membrane (Cytiva) via electroblotting overnight in 0.5 × TBE at 200 mA at 4°C. RNA was fixed to the membrane by ultraviolet (UV) irradiation for 2 min at 80°C for 1 h (UVP HL-2000 HybridLinker). The RNA was hybridized with 100–500 ng of the probe overnight at 52°C and washed twice each with buffer 1 (2 × SSC, 0.1% SDS) and buffer 2 (0.2 × SSC, 0.1% SDS). For the probes, the α-satellite sequence was ligated into a T-vector and identified via sequencing. The probes were amplified by PCR from the T-vector containing the α-satellite sequence and then transcribed with T7 RNA polymerase (Thermo Scientific) using DIG RNA labeling Mix (Roche). The RNAs were then detected using the DIG Northern starter kit (Roche) according to the manufacturer's protocol. Images were taken and processed with an Amersham ImageQuant 800 imager (Cytiva).

Cell cycle synchronization

RPE1 cells were synchronized with a double thymidine block. Thymidine (5 mM, Sigma) was added for 16 h, followed by 8-h incubation in fresh DMEM medium. After a second thymidine block for 16 h, cells were either released into fresh DMEM medium for cell cycle assays or released into medium supplemented with 20 ng/mL nocodazole for 8 h to enrich mitotic cells. The cell cycle distribution was measured using a cell cycle assay kit (FineTest) according to the manufacturer's instructions. After being stained with propidium iodide (PI) reagent at 4°C for 30 min in the dark, the DNA content of the cells was measured by flow cytometry (CytoFLEX, Beckman Coulter).

Single-molecule RNA fluorescence *in situ* hybridization

Single-molecule RNA fluorescence *in situ* hybridization (smFISH) was performed as previously described [33, 34]. The sequences of the hybridization chain reaction (HCR) probes and amplifiers are provided in Supplementary Table S1. Briefly, the cells were seeded on microscope cover glasses (NEST) and synchronized to mitosis with thymidine and nocodazole. After three washes with Dulbecco's phosphate-buffered saline(DPBS, Gibco), the cells were fixed for 10 min using methanol with 25% acetic acid. Before hybridization, the cells were washed twice with DPBS and permeabilized overnight in 70% ethanol at –20°C. The hybridization and amplification steps were performed following the previously reported two-stage multiplexed *in situ* hybridization protocol [33]. The cells were then stained with DAPI (Sigma) and mounted with Fluroshield (Sigma). Images were taken and processed with the LSM 980 confocal system (Zeiss).

For control experiments, the loss of smFISH signals was visualized upon RNase (Thermo) treatments. Cells were treated with 10 U/mL of RNase A (in 50 mM Tris-HCl, pH 7.5, 2 mM EDTA), RNase TI (in 50 mM Tris-HCl, pH 7.5, 2 mM EDTA), or RNase III (in 50 mM NaCl, 10 mM Tris-HCl, pH

7.9, 10 mM $MgCl_2$, 1 mM DTT) for 0.5 hr at 37°C before the probe hybridization step.

Chromatin isolation by RNA purification and sequencing

Chromatin isolation by RNA purification (ChIRP) was performed as previously described with minor modifications [35, 36]. Briefly, cells were fixed with 1% glutaraldehyde (in phosphate-buffered saline (PBS)) for 10 min and quenched with 0.125 M of glycine for 5 min at room temperature. Fixed cells were pelleted and washed once with PBS, and then lysed in nuclear lysis buffer (50 mM Tris-HCl, pH 7.0, 10 mM EDTA, 1% SDS, supplemented with protease inhibitor (Roche), RNase inhibitor (Abclonal), DTT, and PMSF) on ice for 10 min. The cell lysate was sonicated for 15 min (30 s on, 30 s off, Diagenode Bioruptor plus) in a 4°C water bath and centrifuged for 15 min at 12 000 g to remove the insoluble fraction. Chromatin was diluted in two volumes of hybridization buffer (50 mM Tris-HCl, pH 7.0, 750 mM NaCl, 1 mM EDTA, 1% SDS, 15% formamide, supplemented with protease inhibitor, RNase inhibitor, DTT, and PMSF). Six biotinylated probes were generated and split into two independent odd and even probe pools based on their relative positions along the α-satellite. The sequence information is provided in Supplementary Table S1. Biotinylated probes were mixed with the diluted chromatin and subjected to an end-to-end rotation at 37°C for 4 h. M-280 Streptavidin Dynabeads (Invitrogen) were blocked with 500 ng/μL yeast tRNA and 1 mg/mL bovine serum albumin (BSA) before being added to the probe-chromatin mixture. After rotating at 37°C for 2 h, the M-280 beads were washed five times with wash buffer (2 × SSC, 0.5% SDS, supplemented with protease inhibitor and RNase inhibitor) before being subjected to RNA and DNA elution.

Sequencing was performed on Illumina Novaseq 6000 (Novogene). Analysis of ChIRP-seq was performed as previously described [35]. Briefly, sequencing reads were trimmed for adapters using fastp and then mapped to the human genome (hs1) using Bowtie2 [37, 38]. Alignments were shifted toward the 3′ end with MACS2 and normalized to 10 million reads in total [39]. Results from even and odd pools were merged by taking the lower of the two read coverages at each nucleotide across the whole genome. The ChIRP peaks were called from the merged results using MACS2 with the parameter "-g 2.9e9 –broad", and their distribution across the genome was visualized using a Circos plot, which was plotted by the R package Circlize [40, 41].

RNA pull-down

RNA pull-down was performed as previously described with minor modifications [42]. The cells were washed with PBS before UV cross-linking (254 nm, 120 mJ/cm^2). The cells were then lysed in ice-cold RIPA buffer (50 mM Tris-HCl, pH 8.0, 150 mM NaCl, 5 mM EDTA, 1% NP-40, and 0.1% SDS) for 30 min at 4°C with freshly added protease inhibitor (Roche) and RNase inhibitor (Abclonal). After sonication for 10 min (30 s on, 30 s off, Diagenode Bioruptor plus), the cell lysates were centrifuged for 15 min at 12 000 g to remove the insoluble fraction. Thereafter, 100 pmol of the biotinylated oligo probes were incubated with the supernatant for 2 h at room temperature. The sequences of 5′-biotinylated oligo probes are provided in Supplementary Table S1. M-280 Streptavidin Dynabeads (Invitrogen) were blocked with 500 ng/μL yeast tRNA and 1 mg/mL BSA before being added to the probe-cell lysate mixture. After incubation for 2 h at room temperature, the M-280 beads were washed twice with RIPA buffer and twice with high salt RIPA buffer (50 mM Tris-HCl, pH 8.0, 500 mM NaCl, 5 mM EDTA, 1% NP-40, and 0.1% SDS).

Protein samples were heated and preserved in protein sample buffer (40 mM Tris-HCl, pH 6.8, 1% SDS, 5% glycerol, 0.0003% bromophenol blue, and 0.05 M DTT) and then subjected to western blot or silver staining using a Protein Stains K kit (Sangon Biotech). The silver-staining bands of interest were excised and sent for a gel-based liquid chromatography-tandem mass spectrometric analysis (ProtTech Inc.).

The FLAG-tagged SAF-A isoforms and truncation mutants were cloned into the p3XFLAG-Myc-CMV vector by standard PCR-based cloning. All constructs were verified by sequencing (Supplementary Table S2).

RNA immunoprecipitation

Adherent cells were washed with PBS before UV cross-linking (254 nm, 200 mJ/cm^2). The cells were then lysed in RIPA buffer for 30 min at 4°C with freshly added protease inhibitor and RNase inhibitor. After sonication for 10 min, the cell lysates were centrifuged for 15 min at 12 000 g to remove the insoluble fraction. The supernatant was then incubated with Dynabeads Protein G (Invitrogen), which was preincubated with SAF-A antibody (Abcam, ab180952) for immunoprecipitation. After incubation for 2 h at room temperature, the Dynabeads were washed three times with RIPA buffer and split into two portions for protein and RNA collection. Protein samples were heated and preserved in the protein sample buffer. RNA samples were subjected to TRIzol extraction before being used for RT-qPCR.

For the immunoprecipitation of dsRNA, cells were rinsed twice with PBS and lysed in 2 mL of RIPA buffer. The cell lysates were subjected to sonication for 5 min and subsequently centrifuged at 12 000 g for 15 min to remove the insoluble fraction. The supernatant was incubated with Dynabeads Protein G (Invitrogen), which had been preincubated overnight with the J2 antibody (Sigma, MABE1134) at 4°C. The Dynabeads were then washed twice with RIPA buffer and twice with high salt RIPA buffer. RNA extraction from the washed Dynabeads was performed using TRIzol extraction.

Recombinant protein expression and gel shift assay

Full-length SAF-A was cloned into a pET-28a-c (+) vector (Novagen) carrying an *N*-terminal 6 × His tag using the BamHI and EcoRI restriction sites. SAF-A proteins were expressed in *Escherichia coli* BL21(DE3) cells. Cells harboring the pET-28a-c (+) vectors were cultured in LB medium at 37°C until the OD600 reached approximately 0.6 before inducing protein expression. After adding 1 mM IPTG, the cells were cultured at 30°C for a further 20 h. The harvested cells were resuspended in lysis buffer (20 mM Tris-HCl, 400 mM NaCl, 50 mM imidazole, pH 7.5) and lysed by sonication for 10 min (30 s on, 30 s off, Diagenode Bioruptor plus) at 4°C. Recombinant proteins were purified using HisTrap affinity columns (Cytiva) according to the recommended instructions.

Single-stranded RNAs were transcribed *in vitro* using the TranscriptAid T7 High Yield Transcript Kit (Thermo) according to the manufacturer's instructions. Equal molars of sense and antisense transcripts were mixed in the annealing buffer

(10 mM Tris-HCl, pH 8.0, and 20 mM NaCl). The mixture solution was heated to 95°C for 5 min and cooled slowly down to room temperature to anneal the double-stranded RNA. The template vectors for protein expression and RNA transcription are provided in Supplementary Table S2.

In vitro expressed RNA (1 μg) and protein (500 ng) were mixed in the binding buffer (20 mM Tris-HCl, pH 8.0, 15 mM NaCl, 2.5 mM $MgCl_2$, and 1% Tween-20) and incubated at 37°C for 30 min. Samples were separated on native agarose gels and post-stained with GelRed (Biosharp) for 10 min before imaging.

Immunofluorescence

Adherent cells were grown on microscope cover glasses (NEST) in six-well plates and synchronized to mitosis with thymidine and nocodazole. After washing three times with PBS, the cells were fixed for 10 min using methanol with 25% acetic acid. Following a further three washes with PBS, the cells were permeabilized with 0.5% Triton X-100 in ice-cold PBS for 20 min. After two washes with 0.05% Tween-20 in PBS (PBST), the cells were blocked in PBST with 1% BSA for 1 h at room temperature. Primary antibodies were diluted with the blocking buffer. The information on antibodies used is provided in Supplementary Table S3. CREST is a mixture of anti-centromere antibodies derived from human CREST (Calcinosis, Raynaud's syndrome, Esophageal dysmotility, Sclerodactyly, Telangiectasis) patient serum [43]. The cells were incubated overnight with the primary antibodies at 4°C, followed by three washes with PBST. Thereafter, the slides were incubated with the corresponding secondary antibodies for 2 h and washed with PBST three times at room temperature. Finally, the cells were stained with DAPI (Sigma) and mounted with Fluroshield (Sigma). Images were taken and processed using the LSM 980 confocal system (Zeiss).

Western blot

Protein samples were denatured at 95°C for 5 min in protein sample buffer (40 mM Tris-HCl, pH 6.8, 1% SDS, 5% glycerol, 0.0003% bromophenol blue, and 0.05 M DTT) before loading onto sodium dodecylsulphate-polyacrylamide gel electrophoresis for separation. Proteins were then transferred to polyvinylidene fluoride (PVDF) membranes (Millipore), and incubated with the corresponding antibodies followed by an ECL western blotting protocol (Thermo). Information on the antibodies used is provided in Supplementary Table S3. Images were taken and processed with an Amersham ImageQuant 800 imager (Cytiva).

To inhibit Aurora kinases, 2.5 μM of TC-S7010 (MedChemExpress) and 0.25 μM of AZD1152 (MedChemExpress) were added to the culture medium 0.5 h before sample collection [44, 45].

CUT&tag

The CUT&Tag assay was performed using the Hyperactive Universal CUT&Tag Assay Kit for Illumina Pro (Vazyme) according to the manufacturer's recommendations. Specifically, 100 000 cells were immobilized and permeabilized on ConA magnetic beads. The primary antibody was added and incubated overnight at 4°C. After washing with Dig-wash buffer, the secondary antibody was added and incubated for 1 h at room temperature. After washing three times with Dig-wash buffer, 100 μL of Dig-300 buffer containing 0.04 μM pA/G-Tnp Pro was added to the sample. Samples were incubated at room temperature for 1 h and then washed three times with Dig-300 buffer. Samples were then fragmentized in 50 μL of TTBL buffer for 1 hr at 37°C before 0.25 pg DNA spike-in was added to each sample. Then, 25 μL DNA Extract Beads Pro was added to each sample and incubated at room temperature for 20 min to extract the DNA fragments. DNA samples were amplified for 15 cycles using TruePrep Index Kit (Vazyme) and products were purified by VAHTS DNA Clean Beads (Vazyme) for library preparation. Sequencing was performed on Illumina Novaseq 6000 (Novogene). Sequencing reads were trimmed for adapters using fastp and mapped to a combined genome index comprising both the spike-in sequence and the human genome (hs1) using Bowtie2. Read counts mapping to the spike-in sequence were used to generate normalization factors. The alignments to the human reference genome (hs1) were normalized using these spike normalization factors and then converted into bigWig files for visualization using bedtools and bedGraphToBigWig. The peaks were called using MACS2 as described in the "Chromatin Isolation by RNA Purification and Sequencing" section above.

Ethynyl-uridine-labeled RNA sequencing

The Click-iT Nascent RNA Capture Kit (Invitrogen) was used to capture the nascent RNAs. Briefly, RPE1 cells were incubated with 0.5 mM 5-ethynyl-uridine (EU) for 1 h before total RNA was extracted using TRIzol reagent (Invitrogen). The EU-labeled RNAs were biotinylated and captured according to the manufacturer's instructions. RNAs captured on Dynabeads MyOne Streptavidin T1 served as the templates for cDNA synthesis using SuperScript VILO cDNA synthesis kit (Invitrogen). Double-stranded cDNA was synthesized with the Second Strand cDNA Synthesis Kit (Invitrogen) and purified by the PureLink PCR Micro Kit (Invitrogen) as recommended by the manufacturer. Sequencing was performed on Illumina Novaseq 6000 (Novogene). Raw reads were trimmed for adapters using fastp, and the clean reads were then mapped to the human reference genome (hs1) using Bowtie2. The counts of reads mapping to annotated α-satellite transcripts were obtained with bedtools, followed by normalization by read depth.

Co-immunoprecipitation

The cells designated for co-immunoprecipitation (Co-IP) were harvested using trypsin-EDTA (Gibco) and washed twice with PBS. The cell pellet was lysed with lysis buffer (50 mM Tris-HCl pH7.5, 150 mM NaCl, 1% NP-40, supplemented with the Protease Inhibitor Cocktail (Transgene), Phosphatase Inhibitor Cocktail (Transgene), and 1 mM DTT) for 15 min at 4°C. The cell lysate was sonicated for 5 min (30 s on, 30 s off, Diagenode Bioruptor plus) in a 4°C water bath, followed by centrifuge for 15 min at 12 000 g to remove the insoluble fraction. The supernatant was incubated with specific antibodies or IgG overnight and then with Protein G Dynabeads (Invitrogen) for 2 h at 4°C. The Dynabeads were washed five times with the lysis buffer. Protein samples were heated and preserved in the protein sample buffer.

Quantification and statistical analysis

All cellular and biochemical experiments were repeated at least three times. Error bars in the figures represent the standard deviation (SD). All image processing and quantification

were performed using Image J or ZEN black as stated in the corresponding methods. N indicates the number of mitotic cells quantified in each experiment. Statistical analyses were performed using GraphPad Prism 8. Statistical significance was calculated using the two-tailed unpaired Student's t-test when two independent groups were compared. Differences were considered statistically significant when $P < 0.05$. For the CUT&Tag analysis, the comparison of peak enrichment was analyzed using the Wilcoxon rank-sum test.

Results

α-Satellite RNA is dynamically expressed during the cell cycle

We began by examining α-satellite RNAs with northern blots, and it was found that in human RPE1 and HEK293 cells, α-satellite transcription occurred bidirectionally (Fig. 1A and B, and Supplementary Fig. S1A). Northern blot results demonstrated that the α-satellite transcripts range from 100 nt to more than 2000 nt, and a comparable amount of sense and antisense transcripts were observed (Fig. 1B). Therefore, we suspected that α-satellite transcripts from both strands could form RNA duplexes. RNA immunoprecipitation (RIP) using the J2 antibody, which is specific for double-stranded (ds) RNA, revealed that bidirectional transcripts of α-satellite tandem repeats formed α-satellite dsRNAs *in vivo* (Fig. 1C) [46, 47]. Strand-specific RT-qPCR demonstrated significant enrichment of both sense and antisense α-satellite RNAs in J2 RIP compared to the negative control IgG (Fig. 1C). To exclude the theoretical possibility that dsRNA was formed during the immunoprecipitation processes, we further visualized the α-satellite RNA by smFISH. When RPE1 cells were pre-treated with RNase A, the signal was abolished (Fig. 1D); however, treating the cells with either RNase III (dsRNA-specific endoribonuclease) or RNase TI (ssRNA-specific endoribonuclease) results in a decrease, but not the complete abolishment of smFISH signals. These results suggested the existence of both single- and double-stranded α-satellite RNAs *in vivo*.

To assess the expression of α-satellite RNA during the mitotic cell cycle, RPE1 cells were synchronized via a double thymidine block. Upon release into the cell cycle, the distribution of RPE1 cells across different cell cycle phases was analyzed using flow cytometry (Fig. 1E), while the levels of α-satellite RNAs were quantified by RT-qPCR (Fig. 1F). The specificity of the primers was verified by the reduction of PCR products in siRNA knockdown samples and through Sanger sequencing of the amplicons (Supplementary Fig. S1B and S1C). We found that the cellular level of α-satellite RNA showed a burst increase during mitosis and decreased as cells progressed through G1 and into the S phase (Fig. 1E and F). A similar analysis was performed in mouse N2a cells, and elevated amounts of major satellite RNA, but not minor satellite RNA, were observed in the mitotic N2a cells (Supplementary Fig. S2). The activation of α-satellite RNA transcription was corroborated by the capture of nascent RNA utilizing ethynyl-uridine-labeled RNA sequencing (EU-RNA-seq). Cells in the G1, S, G2, and M phases were harvested at 3, 6, 8, and 11 h after the double thymidine block and release, respectively, and EU was introduced into the culture medium 1 h before cell collection. Compared with asynchronous cells, those in the G2 and M phases exhibited significantly elevated levels of nascent α-satellite RNA, which indicates active α-satellite transcription during mitosis (Fig. 1G). However, the transcriptional activation was not uniformly distributed across the α-satellite repeat regions. Specifically, in the M phase cells, 40% of the α-satellite repeats demonstrated significant upregulation in transcriptional relative to asynchronous cells (fold change > 2) (Fig. 1H). Conversely, 36% and 24% of the α-satellite repeat regions exhibited no change ($0.5 \leq$ fold change ≤ 2) or downregulation (fold change < 0.5) during mitosis, respectively.

These findings suggest that α-satellite RNAs exhibit dynamic expression patterns throughout the mitotic cell cycle and are actively transcribed during mitosis, with comparable levels of bidirectional transcripts that can form dsRNA.

Mitotic transcription of α-satellite RNAs requires activities of aurora kinases

The regulators of the cell cycle dynamic expression of α-satellite RNAs were then investigated. Aurora kinases, including Aurora kinase A (AURKA) and Aurora kinase B (AURKB), are key orchestrators of mitosis and are localized at the centromeres when α-satellite RNAs were transcribed [48, 49]. AURKA plays a vital role in centrosome maturation and spindle assembly, thereby facilitating accurate chromosome alignment and segregation during mitosis [48]. The autophosphorylation at Thr288 is essential for the catalytic activation of AURKA [50]. AURKB, on the other hand, is critical for chromosome segregation and the spindle assembly checkpoint, thereby ensuring that the cells do not proceed to anaphase until all chromosomes are properly attached to the spindle apparatus [49]. Its kinase activity is required for the autophosphorylation of Thr232 loci [51].

To investigate the influence of the Aurora kinases on α-satellite RNA expression, we evaluated the effect of inhibiting AURKA and AURKB using the selective inhibitors TC-S7010 and AZD1152, respectively [52, 53]. Because both AURKA and AURKB are known as crucial mitosis regulators and play considerable roles in cell cycle progression, the treatment durations and inhibitor concentrations were tested beforehand to minimize the effects of possible cell cycle arrest during Aurora kinase inhibition (Supplementary Fig. S3) [54, 55]. Histone H3 Ser10 phosphorylation (H3S10P), a known substrate of both kinases, was examined as a positive control for the inhibitor treatments [56, 57]. Western blotting demonstrated that both Aurora kinases were specifically activated during the G2-M phase of the cell cycle, thus corroborating the findings of previous studies (Fig. 2A) [58]. Treating cells with 2.5 μM of TC-S7010 for 0.5 h completely abrogated AURKA Thr288 phosphorylation (T288P) without affecting AURKB Thr232 phosphorylation (T232P), while treatment with 0.25 μM AZD1152 substantially diminished AURKB T232P without impacting AURKA T228P, thereby confirming the efficacy and specificity of both inhibitors (Fig. 2A). Treating cells with AZD1152 results in a substantial reduction in the H3S10P levels, thereby indicating the predominant role of AURKB in H3S10P regulation (Fig. 2A and B). Furthermore, an additional decrease in the H3S10P signal was observed in cells treated with both inhibitors, which suggests an additive effect of AURKA and AURKB on H3S10P (Fig. 2A and B). Inhibition of either AURKA or AURKB kinase activity led to a significant decrease in α-satellite RNA levels, especially in the mitotic cells, suggesting both Aurora kinases were involved in regulating the cell cycle dynamic expression of α-satellite RNAs (Fig. 2C).

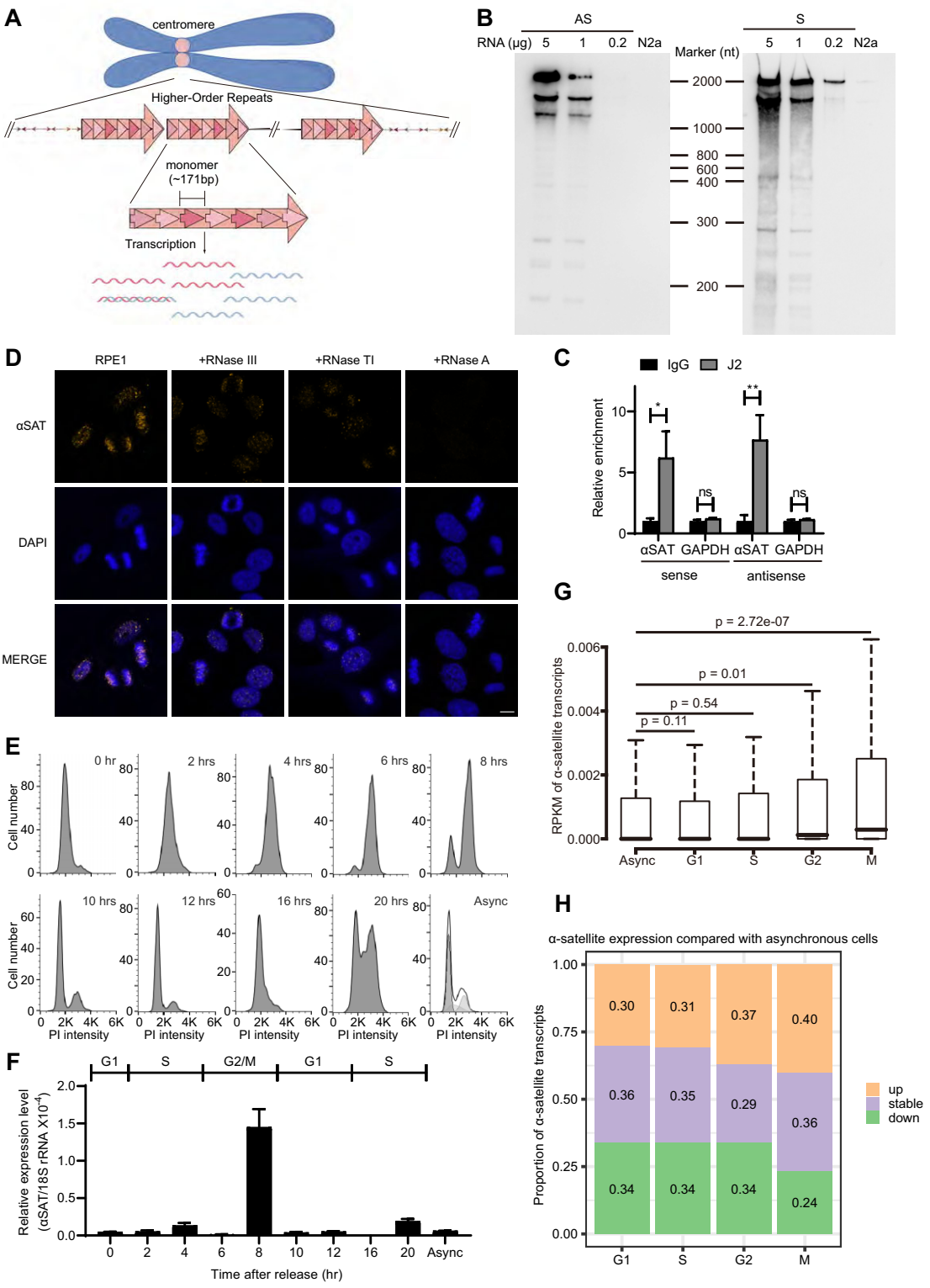

Figure 1. Cell cycle dynamic expression of α-satellite RNAs. (**A**) Scheme representing the genomic organization of α-satellite and the transcription of α-satellite RNAs. Wiggle lines represent α-satellite RNAs originating from both strands. (**B**) Northern blot of α-satellite RNAs in RPE1 cells. S, sense transcripts; AS, antisense transcripts. RNAs from mouse N2a cells serve as negative control. (**C**) Immunoprecipitation with J2 antibody against double-stranded RNAs follows with strand-specific RT-qPCR. The enrichment is relative to immunoprecipitation with the IgG antibody. The error bars represent SD, $n = 3$. Statistical significance is calculated using two-tailed unpaired t-tests and is reported as $P < 0.05$ *, $P < 0.01$ **, $P > 0.05$ ns. (**D**) SmFISH of α-satellite RNA in RPE1 cells pre-treated with RNases. Scale bar, 10 μm. (**E**) Cell cycle distribution of RPE1 cells determined by propidium iodide (PI) staining followed by flow cytometry. Asynchronous cells (Async) serve as the control. (**F**) RT-qPCR showing expression levels of α-satellite RNAs in cells at indicated time points after release. The predominant cell cycle stage of each time point is indicated on top. The error bars represent SD, $n = 3$. (**G**) EU-RNA-seq showing nascent α-satellite RNA levels in different cell cycle stages. Unpaired t-tests are used. (**H**) The stacked bar graph depicts the proportion of α-satellite repeats that showed upregulation, downregulation, or remain stable of transcription within the mitotic cell cycle. Asynchronous cells (Async) serve as the control..

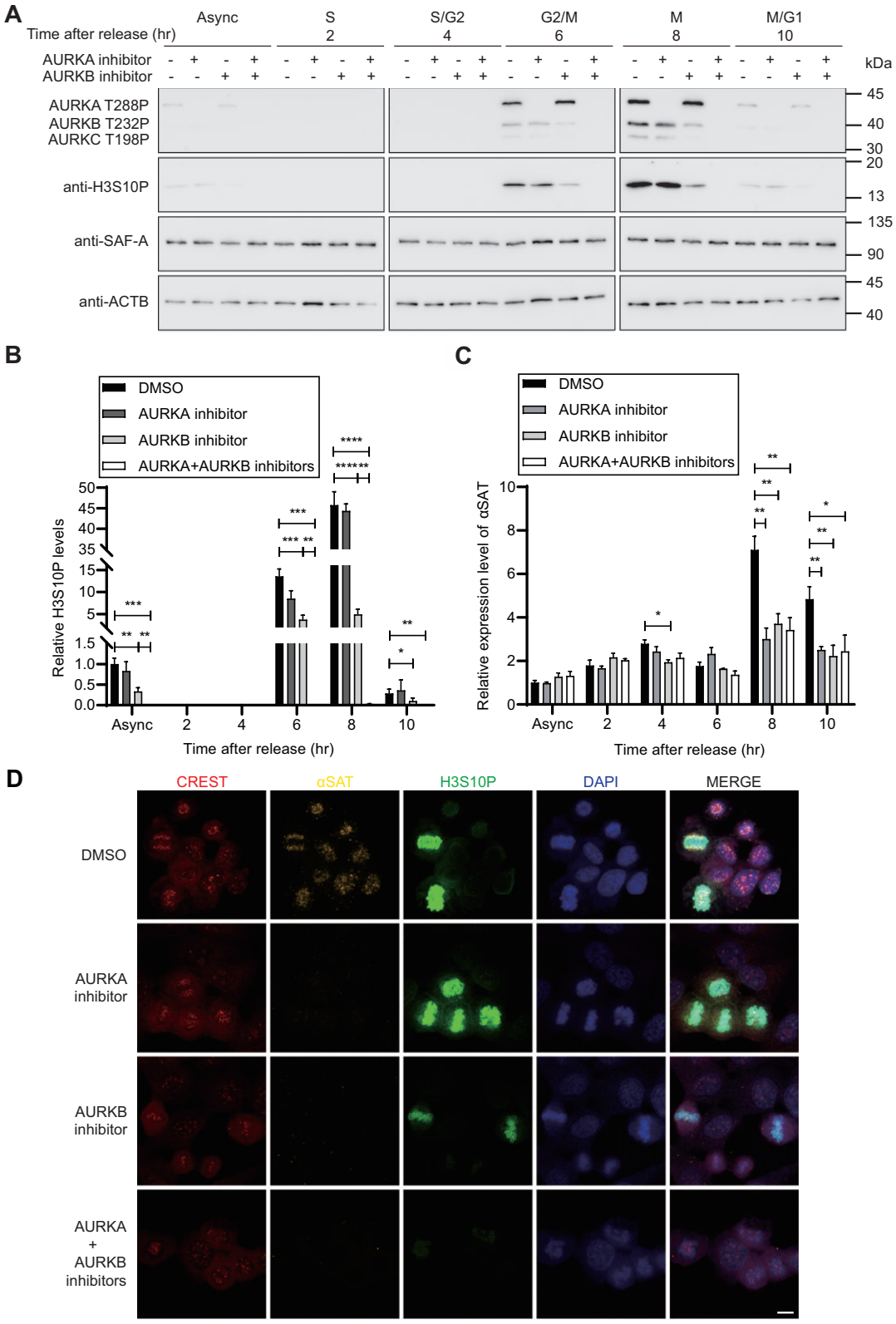

Figure 2. Aurora kinases regulate the expression of α-satellite RNA. (**A**) Representative western blotting demonstrates the inhibition of Aurora kinases in synchronized cells. AURKA inhibitor, TC-S7010 (2.5 μM); AURKB inhibitor, AZD1152 (0.25 μM). H3S10P serves as positive control; ACTB, β-actin, serves as the internal loading control. (**B**) Quantification of H3S10P western blot in (A). (**C**) RT-qPCR analysis showing relative α-satellite RNA levels upon Aurora kinase inhibition. DMSO, no drug control. Results are normalized to Async no drug control. The error bars represent SD, $n = 6$. Statistical significance is calculated using unpaired t-tests and is reported as $P < 0.05$ *, $P < 0.01$ **, $P < 0.001$ ***, $P < 0.0001$ ****. (**D**) Representative images of α-satellite RNAs (αSAT) smFISH, CREST, and H3S10P IF in cells treated with Aurora kinase inhibitors. Scale bar, 10 μm.

Moreover, we assessed the impacts of Aurora kinase inhibition on the cellular levels of α-satellite RNAs using confocal microscopy. CREST serum, which stains the inner kinetochore regions, was used to visualize the centromeres (see methods for details) [43]; while H3S10P was concurrently immunostained to demonstrate Aurora kinase inhibition (Fig. 2D). Under Aurora kinase inhibitors treatment, a drastic reduction in α-satellite RNA smFISH signals was observed (Fig. 2D). It is worth noting that, different from the additive inhibitory effect observed of AURKA and AURKB inhibition on H3S10P, the inhibition of either Aurora kinase resulted in a nearly complete loss of α-satellite RNA smFISH signal, which suggests that the expression of α-satellite RNAs was dependent on the activities of both Aurora kinases.

α-satellite RNAs are centromere chromatin-associated

Next, we proceeded to determine the localization of α-satellite RNA within the mitotic cell cycle. α-Satellite RNAs examined by smFISH predominately colocalized with the CREST IF signals (Fig. 3A). Throughout the cell cycle and during mitosis, α-satellite RNA transcripts remained centromere chromatin-associated (Fig. 3A), while it was reported that most of the caRNAs were released from chromatin and underwent relocalization [32].

We then conducted ChIRP-seq experiments targeting α-satellite RNA to further substantiate its association with centromeric chromatin. For comparison, we analyzed the publicly available CENP-A CUT&RUN dataset and the H3K9me3 ChIP-seq dataset in RPE1 cells [37, 59]. The genome-wide comparison revealed that the ChIRP-seq peaks of the α-satellite RNAs significantly overlapped with CENP-A CUT&RUN signals, thereby confirming that α-satellite RNAs were predominantly localized within the centromere regions of all chromosomes (Fig. 3B–D). In a more detailed classification of the chromosome regions, it was observed that 83.50% and 85.25% of α-satellite RNA ChIRP-seq peaks were localized to the centromere region in both the asynchronous and synchronized M phase cells, respectively (Fig. 3E). Notably, the shorter p-arms appeared to bind more α-satellite RNAs compared with the q-arms, which was likely attributed to the presence of acrocentric satellite repeats that were specifically located in the short arms of acrocentric chromosomes (Fig. 3E). Sequence analyses of the α-satellite RNA binding sites further revealed that over 95% of α-satellite RNAs were specifically associated with DNA sequences that were annotated as α-satellite, thus underscoring the high specificity of α-satellite RNA binding sites (Fig. 3F). Collectively, these results demonstrate that α-satellite RNAs are specifically associated with centromeric chromatin throughout the entire mitotic cell cycle.

α-satellite RNAs interact with SAF-A

We searched for α-satellite RNA binding proteins via an RNA pull-down assay in asynchronous RPE1 cells using probes against α-satellite RNAs (Fig. 4A). Silver staining revealed the presence of several distinct protein bands coprecipitated with α-satellite RNAs (Fig. 4A). These distinct silver-staining bands, which were pulled down by both sense and antisense α-satellite probes, were excised and subsequently analyzed by gel-based liquid chromatography-tandem mass spectrometry analysis. This analysis identified several putative α-satellite RNA binding proteins, including the important nuclear scaffold protein SAF-A (Fig. 4A, Supplementary Table S4). Considering the crucial roles and regulatory mechanisms of SAF-A in both interphase and mitotic cells, we focused on this protein for further investigation.

The coprecipitation of SAF-A with α-satellite RNA was verified first using RNA pull-down followed by western blot analysis (Fig. 4A). To further confirm the physical association between SAF-A and α-satellite RNAs, RIP was performed using an SAF-A antibody (Fig. 4B). α-Satellite RNA was enriched in the SAF-A immunoprecipitation compared with the IgG control, at relative enrichments that were comparable to those of snRNA U5 and U6, which are established non-coding RNAs that interact with SAF-A [24]. The major and minor satellite sequences in mice are considered analogous to human α-satellites [1, 8]. Utilizing biotinylated oligonucleotides targeting major and minor satellite RNAs, we identified an interaction between SAF-A and major satellite RNAs but not with minor satellite RNAs in mouse N2a cells (Supplementary Fig. S4A and S4B). Consistently, RIP assays demonstrated that endogenous major satellite RNA was significantly enriched using a SAF-A antibody (Supplementary Fig. S4C). In contrast, minor satellite RNA did not exhibit significantly higher enrichment with the SAF-A antibody than that of the negative IgG control (Supplementary Fig. S4C). These findings further substantiate that, in mice, SAF-A interacts specifically with major satellite RNAs but not with minor satellite RNAs.

SAF-A contains four conserved domains (Fig. 4C): SAP (SAF/Acinus/PIAS motif), which is known as the DNA binding domain; SPRY (splA and ryanodine receptor), which is known as a protein interaction module; AAA + domain, which is a conserved ATP-binding domain found in many ATPases; and RGG domain, which is an RNA-binding domain. The two SAF-A isoforms, designated as isoform a and isoform b, differ by only 19 amino acids within the linker region between the SAP and SPRY domains (Fig. 4C) [60]. Despite being situated in a less structured region, the presence of these amino acids appears to substantially influence the SAF-A 3D structure, as predicted by AlphaFold (Supplementary Fig. S5A) [61]. Further analysis using PONDR identified that amino acids 212–230 reside within an intrinsically disordered region (IDR) (Supplementary Fig. S5B) [62]. Using mRNA expression data from GTEx (Version 10), we compared the expression levels of isoforms a and b across various human tissues. In all human tissues analyzed, isoform a is predominantly expressed (Supplementary Fig. S6A). Given that α-satellite RNA is expressed in a cell cycle-dependent manner, we investigated whether the SAF-A expression level was similarly regulated by the cell cycle. Because of the current limitation in the availability of antibodies to distinguish between SAF-A isoforms, we assessed the mRNA levels of both isoforms using isoform-specific primer pairs (Supplementary Fig. S6B). The results indicated that in RPE1 cells, both isoforms were expressed throughout the mitotic cell cycle. Notably, there was a significant upregulation (fold change > 2 relative to asynchronous cells) of SAF-A isoform a mRNA during the late S and early G1 phases of the cell cycle. In contrast, isoform b mRNA levels remained relatively low and exhibited less fluctuation throughout the cell cycle (Supplementary Fig. S6B).

We incubated *in vitro* transcribed α-satellite RNAs with recombinant SAF-A and found via an electrophoretic mobility shift assay that both sense and antisense α-satellite

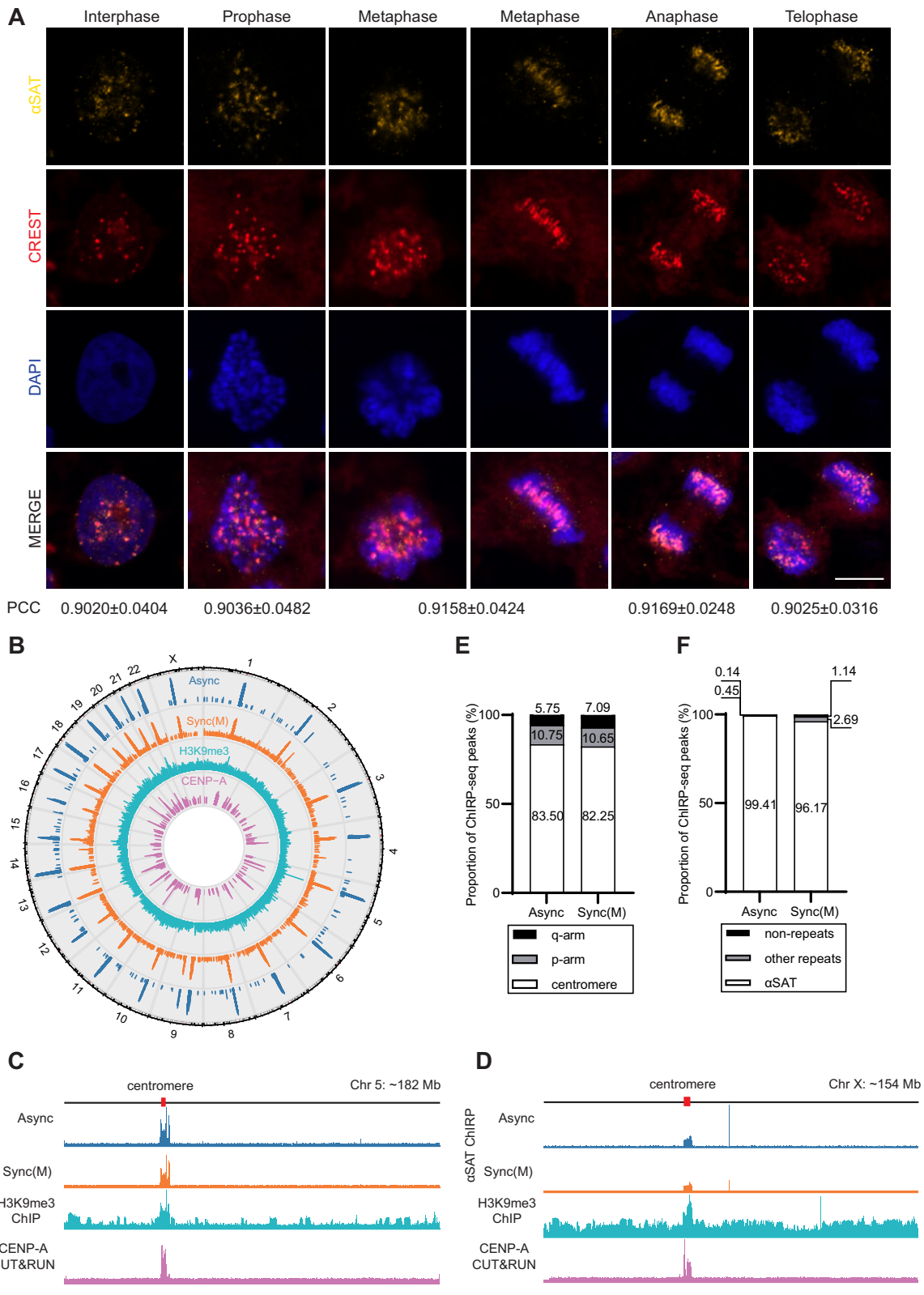

Figure 3. α-satellite RNA is centromere chromatin-associated in the mitotic cell cycle. (**A**) Representative images of α-satellite RNA smFISH and CREST IF in RPE1 cells. PCC, Pearson correlation coefficient. Scale bar, 10 μm. (**B**) Circos plot showing the genome-wide binding sites of α-satellite RNA. Items displayed from the outer to the inner layer are α-satellite RNA ChIRP-seq in Async cells; α-satellite RNA ChIRP-seq in Sync(M) cells; H3K9me3 ChIP-seq; CENP-A CUT&RUN. (**C**-**D**) Genome browser view of α-satellite RNA ChIRP-seq peaks on (C) chromosome 5 and (D) chromosome X. (**E** and **F**) Distribution of α-satellite RNA ChIRP-seq peaks on (E) chromosome arms and (F) repetitive sequences.

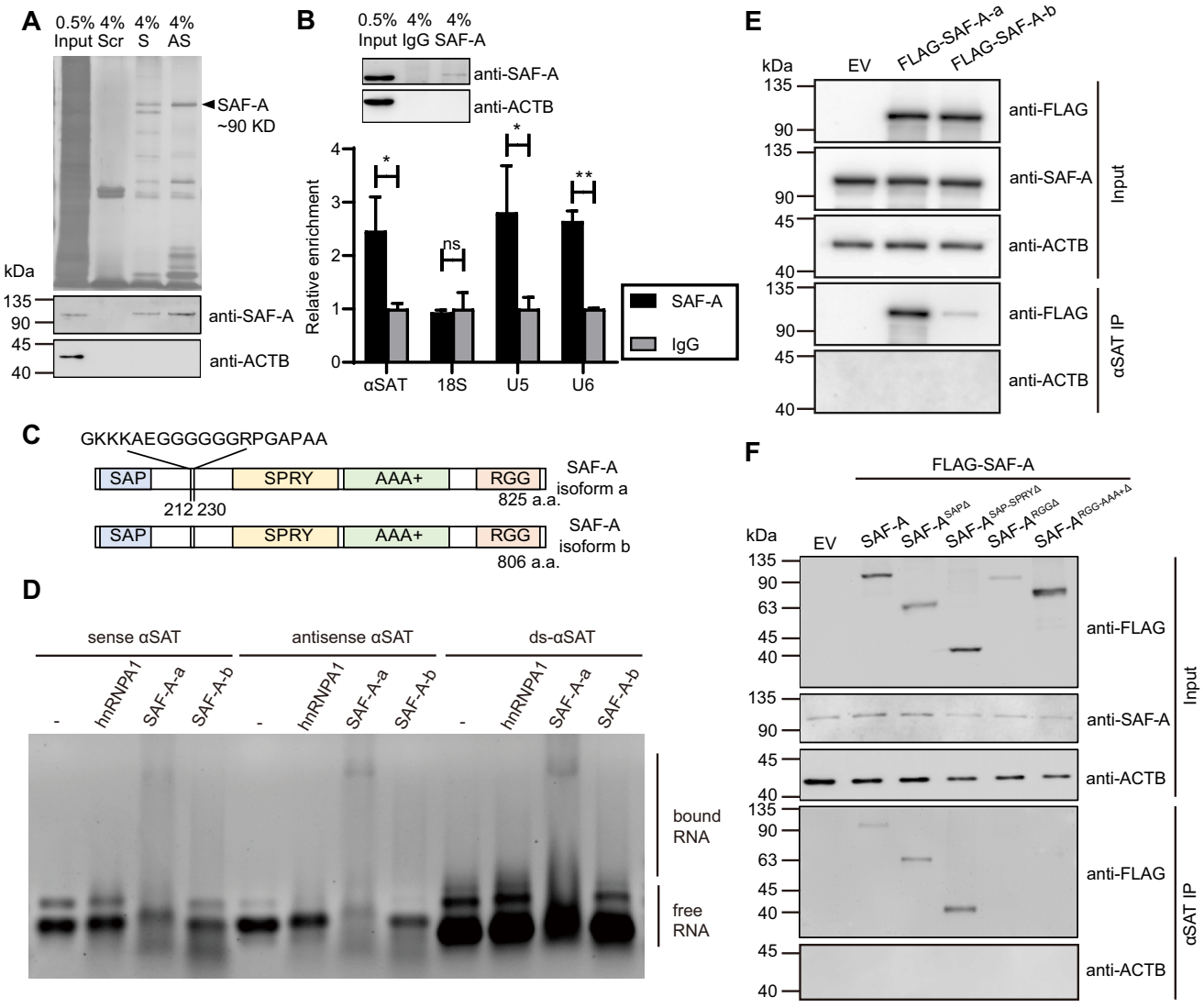

Figure 4. α-Satellite RNA interacts with SAF-A. (**A**) Silver staining and western blot of RNA pull-down in RPE1 cells using α-satellite RNA targeting probes. Scr, scramble; S, sense; AS, antisense. (**B**) RIP with SAF-A antibody and non-specific IgG antibody. Relative enrichments of RNA transcripts are quantified using RT-qPCR. The error bars represent SD, $n = 3$. Statistical significance is calculated using unpaired t-tests and is reported as $P < 0.05$ *, $P < 0.01$ **, $P > 0.05$ ns. (**C**) Schematic diagram of SAF-A domain architecture. The 19 amino acids that are missing in isoform b are indicated above. (**D**) Gel shift assay showing the binding of SAF-A isoforms to α-satellite RNA. -, no protein control; hnRNPA1, no binding control. (E-F) RNA pull-down of (**E**) FLAG-tagged SAF-A isoforms and (**F**) FLAG-tagged SAF-A truncation constructs using biotinylated α-satellite probes. EV, empty vector; anti-SAF-A shows the endogenous SAF-A levels; ACTB, β-actin, serves as the internal loading control.

transcripts interacted with SAF-A isoform a, but showed little interaction with isoform b (Fig. 4D). α-Satellite dsRNA also showed a specific preference toward SAF-A isoform-a (Fig. 4D). To confirm this isoform-specific interaction between SAF-A and α-satellite RNA, FLAG-tagged SAF-A constructs were transfected into RPE1 cells and subjected to an RNA pull-down assay. Consistent with the results of the gel shift assay, α-satellite RNA exhibited a much higher affinity for the SAF-A isoform a (Fig. 4E).

Consequently, domain truncation analysis was performed on isoform a. The FLAG-SAF-A constructs with specific domain truncations were ectopically expressed in RPE1 cells. The ectopic expression of these truncated SAF-A constructs induced slight alterations in the expression level of endogenous SAF-A (fold change < 2 relative to empty vector control), without influencing the α-satellite RNA levels (Supplementary Fig. S7). The affinity of these domain-truncated SAF-A constructs for α-satellite RNAs was evaluated using an RNA pull-down assay (Fig. 4F). The truncation of the RGG domain largely abolished the interaction between SAF-A and α-satellite RNAs, which suggests that RGG was the key domain for α-satellite RNA binding (Fig. 4F). On the other hand, the loss of *N*-terminal SAP and SPRY domains appeared to augment SAF-A's affinity toward α-satellite RNA, suggesting that they might also play a regulatory role in α-satellite RNA-binding (Fig. 4F).

These results collectively indicate that SAF-A engages in physical interactions with α-satellite RNAs. Moreover, the as-

sociation between α-satellite RNA and SAF-A is reliant on the RGG domain of the protein and displays isoform specificity.

Cell cycle-dependent association of α-satellite RNA and SAF-A

We next examined the localization of α-satellite RNAs and SAF-A at different cell cycle stages (Fig. 5A). Immunofluorescence microscopy revealed that SAF-A was broadly distributed within the nucleus during interphase and prophase and exhibited substantial colocalization with centromeres and α-satellite RNAs. However, in metaphase and anaphase, α-satellite RNAs and SAF-A colocalization diminished, as SAF-A was expelled from the mitotic chromosomes (Fig. 5A) [32]. Unlike α-satellite RNAs that are associated with chromosomes throughout the mitotic cell cycle, SAF-A appeared to disassociate from the condensed chromosomes in metaphase and anaphase and then were recruited back during telophase (Fig. 5A).

The chromatin association of SAF-A in asynchronized cells and mitotic cells were further assessed by CUT&Tag. As a prevalent component of the nuclear scaffold, SAF-A demonstrated a widespread association with chromatin, which included a larger region than that of α-satellite RNA (Fig. 5B). Therefore, we performed a permutation test to confirm the colocalization between SAF-A CUT&Tag peaks and α-satellite RNA ChIRP-seq peaks (Supplementary Fig. S8A). This analysis revealed a statistically significant difference ($P < 1 \times 10^{-5}$, permutation test) in α-satellite RNA coverage between SAF-A CUT&Tag peaks and the non-peak control regions in both asynchronous and mitotic cells, underscoring the colocalization of SAF-A and α-satellite RNA. Considering the heterogeneity of α-satellite sequences, we further investigated the potential features that may have influenced their colocalization with SAF-A (Supplementary Fig. S8B, Supplementary Table S5). As previously reported, the SAF-A ChIP-seq peaks frequently coincide with the CTCF motif [22]. Consequently, we analyzed the presence of CTCF motifs within genomic regions that are covered by both α-satellite RNA and SAF-A, as well as covered solely by α-satellite RNA. A higher abundance of CTCF motifs was observed within the regions covered by both α-satellite RNA and SAF-A ($P = 9.02 \times 10^{-7}$ and $P = 4.19 \times 10^{-9}$ in asynchronous and mitotic cells, respectively). In alignment with the immunofluorescence results, a reduction in chromatin-associated SAF-A is evident in mitotic cells (Fig. 5C). Particularly, at centromere regions, there is also a pronounced decrease in centromere-associated SAF-A within mitotic cells (Fig. 5D). Correspondingly, RIP assays utilizing SAF-A antibodies revealed a significant decline in the interaction between SAF-A and α-satellite RNAs during the M phase (Fig. 5E).

Collectively, these results suggest that SAF-A interacts with α-satellite RNAs in a cell cycle-dependent manner. During interphase, both SAF-A and α-satellite RNA are associated with centromeric chromatin. However, during mitosis, SAF-A appears to undergo a dissociation and reassembly process, the majority of SAF-A is disassociated from the mitotic chromosomes and subsequently reestablished upon the mitotic exit.

α-satellite RNAs and SAF-A interference results in mitosis defects

To understand the importance of the dynamic expression and interaction of SAF-A and α-satellite RNA during mitosis, we induce the RNA interfered of α-satellite RNAs using a pair of siRNAs (siASATs), which had been successfully used in previous studies [11]. Compared with the siNC negative control, siASAT-treated cells displayed significant reductions in α-satellite RNA levels, without significantly altering cell cycle progression (Fig. 6A,B, Supplementary Fig. S9A, and S9B). Mitotic cells were stained for tubulin and CREST to determine possible mitotic defects, and cells transfected with siASATs exhibited a significantly elevated frequency of abnormal mitotic phenotypes, particularly chromosome misalignment, chromosome lagging, and multipolar mitosis (Fig. 6A and C). Meanwhile, we knocked down SAF-A in RPE1 cells using a pair of lentiviral vector-based shRNAs without significantly influencing cell cycle progression (Fig. 6D and E and Supplementary Fig. S9C). Similar chromosome misalignment and missegregation phenotypes were observed in SAF-A knockdown cells (Fig. 6D and F). These results demonstrate that both α-satellite RNA and SAF-A are required for maintaining the genome integrity during mitosis.

α-satellite RNA is required for the proper localization of SAF-A during mitosis

The physical interaction between α-satellite RNAs and SAF-A led us to examine whether α-satellite RNA was required for the cell cycle-dependent chromatin association of SAF-A. Therefore, we performed α-satellite RNA knockdown and examined the localization of SAF-A in these cells. In the control cells, SAF-A signals were observed on the chromatin during interphase and prophase, and thereafter SAF-A signals were evacuated from the condensed chromosome region during metaphase and anaphase and then re-localized to this region during telophase (Figs 5A and 7A). In α-satellite RNA knockdown cells, more than 20% of telophase cells exhibited a failure in recruiting SAF-A to the chromatin, which is a significantly higher proportion than that of the control cells (Fig. 7A and B). Meanwhile, approximately 12% of the metaphase cells failed to exclude chromosome-associated SAF-A, which was significantly higher than that in the control cells (Fig. 7A and C). The SAF-A protein levels were not affected by α-satellite RNA knockdown (Fig. 7D). These results indicated that α-satellite RNA was required for the chromosome eviction and loading of SAF-A during mitosis progression. In parallel, we examined the localization of α-satellite RNA following the knockdown of SAF-A with shRNAs (Supplementary Fig. S10). When compared with cells transfected with control shRNAs, cells transfected with shSAF-As did not exhibit any significant changes in the localization of α-satellite RNAs (Supplementary Fig. S10).

We then tested whether α-satellite RNA depletion influenced the nuclear lamina assembly by investigating the recruitment of nuclear lamins. The distribution of lamins within the nucleus is characterized by a distinctive boundary that corresponds to the nuclear membranes (Fig. 8A) [63]. In RPE1 cells, the nuclear lamin boundaries break down at prophase and reassembled in telophase (Fig. 8A). Co-immunoprecipitation assays revealed a direct interaction between SAF-A and the nuclear lamins (Fig. 8B and C). Accordingly, a significant increase in the failure or incomplete assembly of nuclear lamins at the mitotic exit was observed with SAF-A knockdown (Fig. 8D and E). Furthermore, in cells subjected to siASAT knockdown, failure or incomplete assembly of nuclear lamins at the mitotic exit was also significantly increased (Fig. 8F and G).

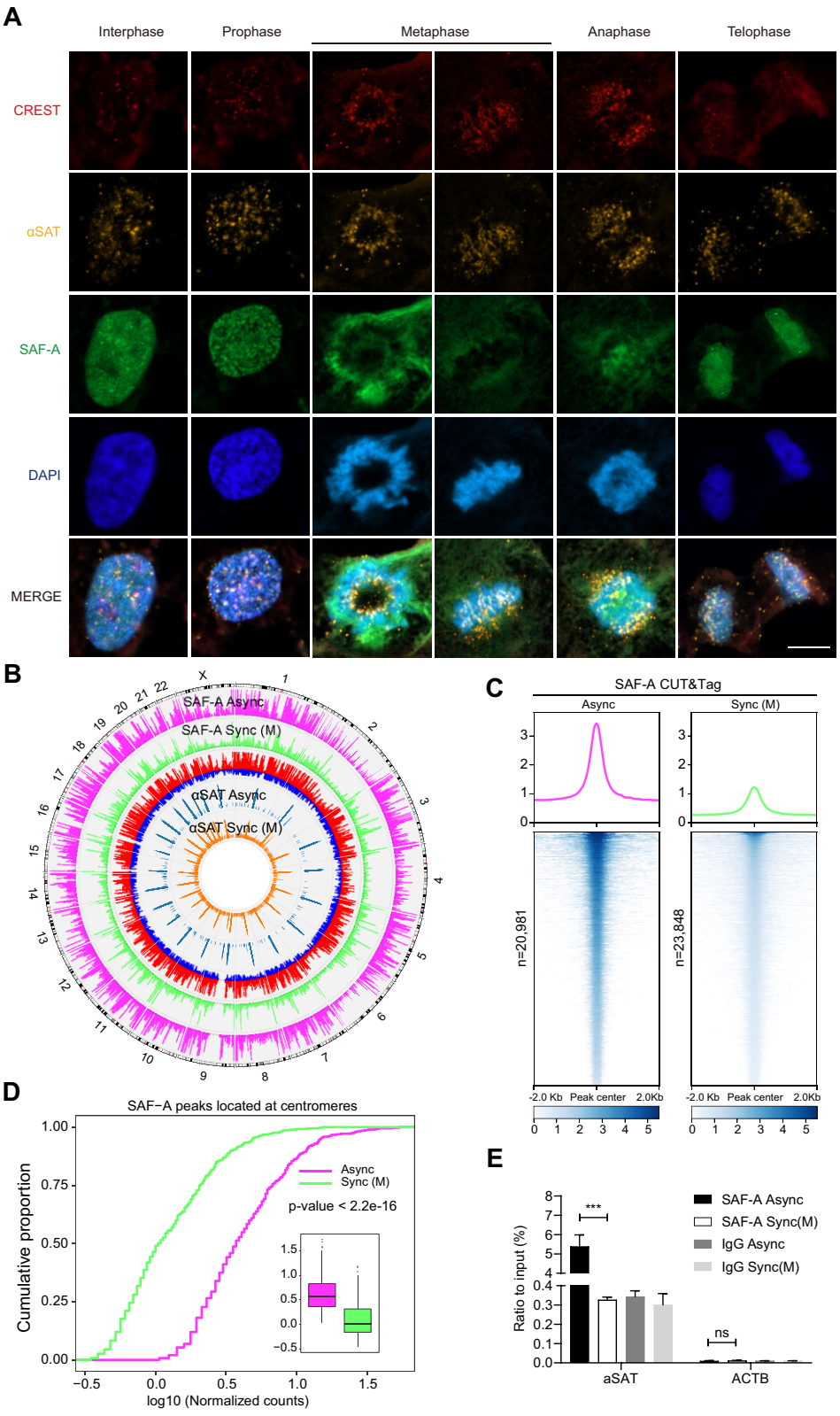

Figure 5. Cell cycle-dependent association of SAF-A and α-satellite RNA. (**A**) Representative images of α-satellite RNA smFISH and SAF-A IF at different cell cycle stages. Scale bar, 10 μm. (**B**) Circos plot showing the chromatin association of SAF-A and α-satellite RNA. Items displayed from the outer to the inner layer are SAF-A CUT&Tag in Async cells, SAF-A CUT&Tag in Sync(**M**) cells, the subtraction of SAF-A CUT&Tag between Async and Sync(M) cells, αSAT ChIRP-seq in Async cells, and αSAT ChIRP-seq in Sync(M) phase cells. Averages of normalized CUT&Tag signals of two independent experiments are shown. (**C**) Pile-up heatmaps and summary plots of SAF-A CUT&Tag signals in Async and Sync(M) cells. (**D**) The cumulative plot and boxplot demonstrate the enrichment of SAF-A CUT&Tag peaks at centromere regions. The P was calculated using the Wilcoxon rank sum test. (**E**) RIP with SAF-A and non-specific IgG antibodies in Async and Sync(M) RPE1 cells. The relative ratio of RNA transcripts was quantified using RT-qPCR. The error bars represent SD, $n = 6$. Statistical significance was calculated using unpaired t-tests and is reported as $P > 0.05$ ns, $P < 0.001$ ***.

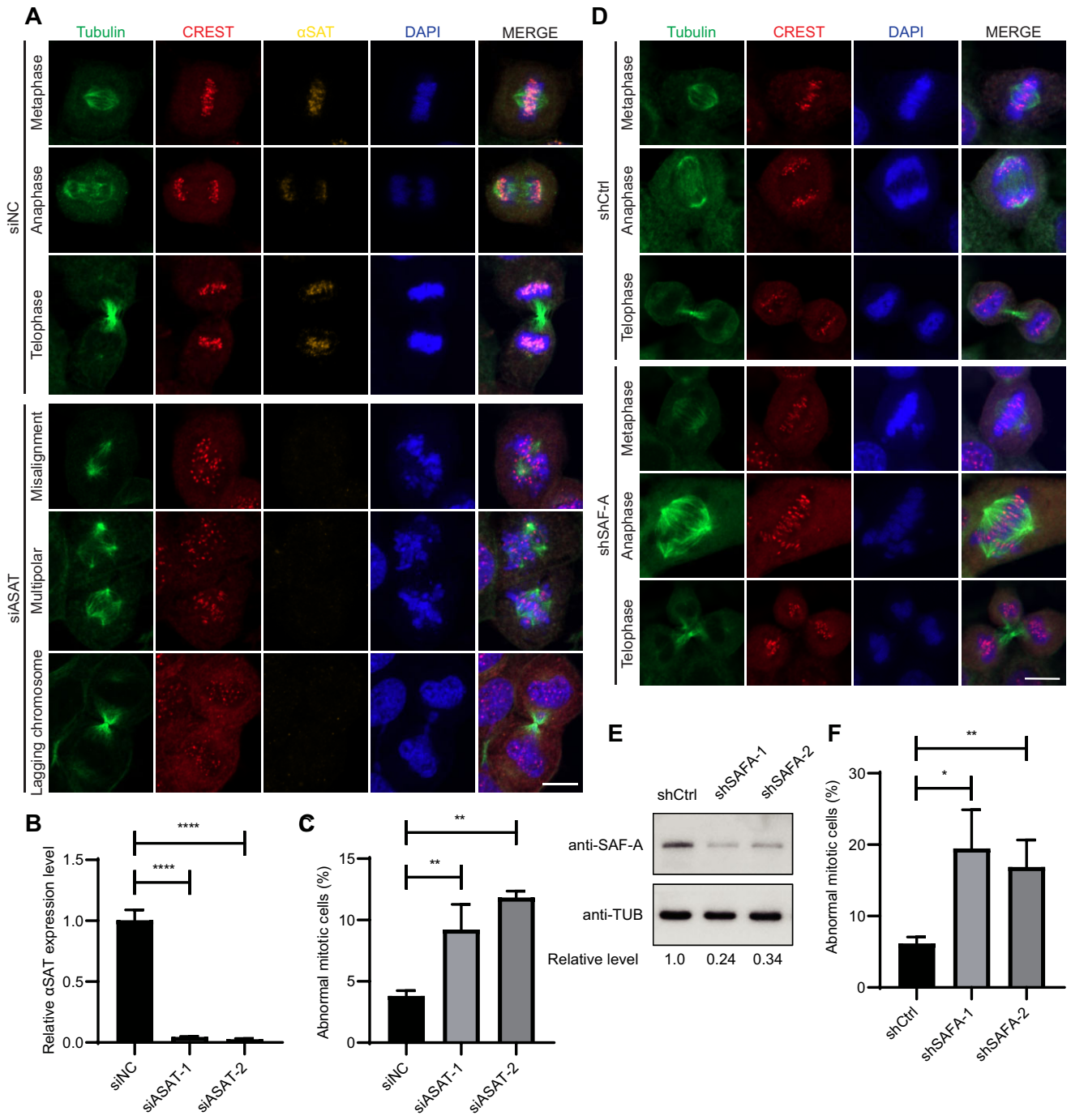

Figure 6. Knockdown of α-satellite RNA or SAF-A leads to chromosome missegregation phenotypes in mitotic cells. (**A**) Representative CREST and tubulin IF images show the chromosome missegregation in mitotic cells after knockdown of α-satellite RNAs with siRNA. Scale bar, 10 μm. siNC, non-specific control siRNA. (**B**) RT-qPCR analysis demonstrating knockdown efficiency of siRNAs against α-satellite RNAs (siASATs) in RPE1 cells. siNC, non-specific control siRNA. (**C**) Percentage of cells displaying abnormal mitotic phenotypes after siRNA transfection. (**D**) Representative CREST and tubulin IF images show the chromosome missegregation in mitotic cells after SAF-A knockdown with shRNA constructs. shCtrl, non-specific control shRNA construct. Scale bar, 10 μm. (**E**) Western blot verifies the shRNA-mediated knockdown of SAF-A. TUB, tubulin, serves as the internal loading control. (**F**) Percentage of cells displaying abnormal mitotic phenotypes after transfected with shRNA constructs. All data were from at least three independent experiments. In each independent experiment, N > 200 mitotic cells were counted. The error bars represent SD. Statistical significance was calculated using unpaired t-tests and is reported as $P < 0.05$ *, $P < 0.01$ **, $P < 0.0001$ ****.

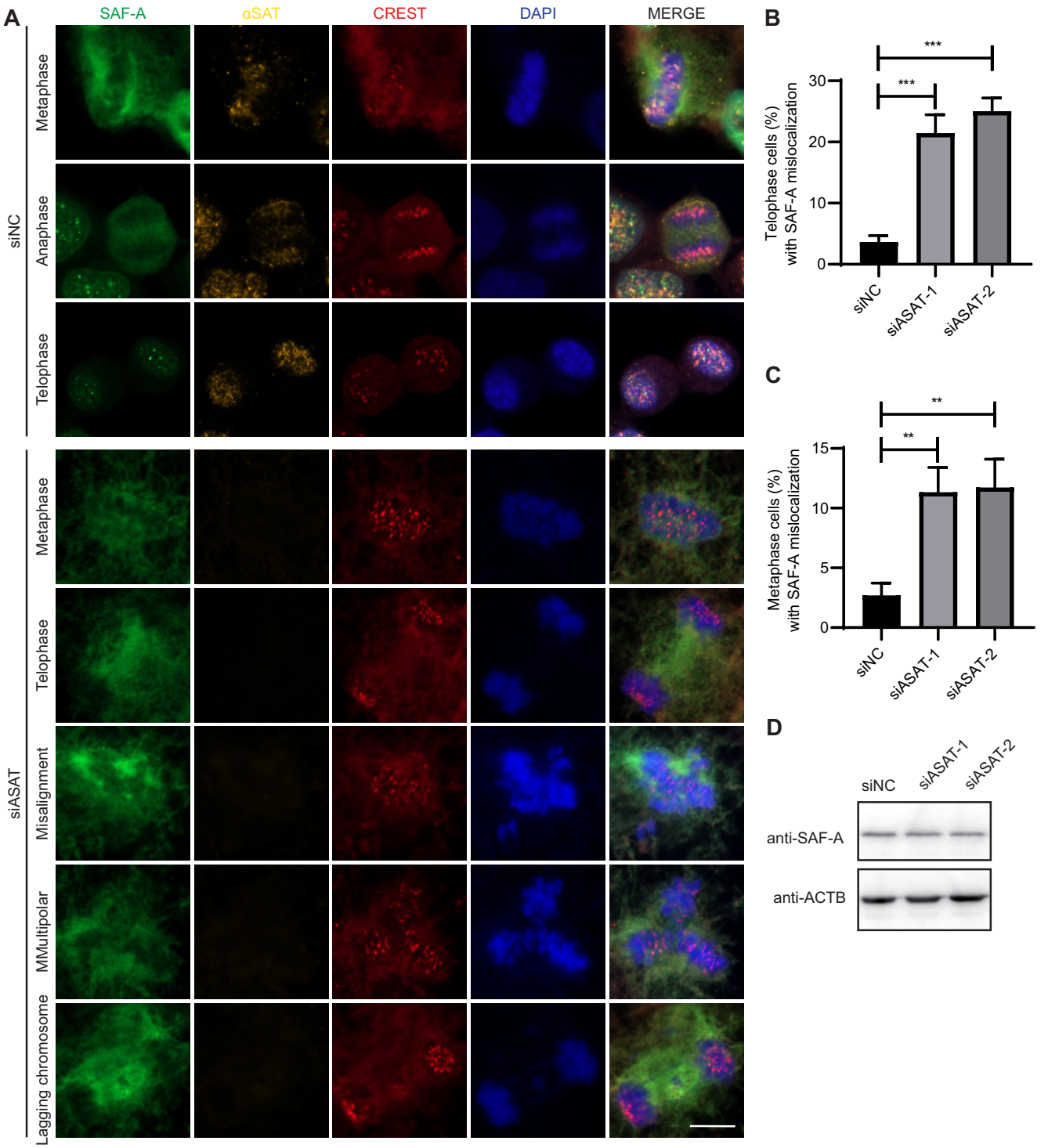

Figure 7. α-Satellite RNA regulates the eviction and reassembly of chromatin-associated SAF-A. (**A**) Representative α-satellite RNA smFISH and SAF-A IF images show the abnormal location of SAF-A after the knockdown of α-satellite RNA with siRNA. Scale bar, 10 μm. (**B**) Percentage of telophase cells displaying abnormal SAF-A localization after siASATs transfection. (**C**) Percentage of metaphase cells displaying abnormal SAF-A localization after siASATs transfection. (**D**) Western blot demonstrates SAF-A protein levels in siASAT transfected cells. ACTB, β-actin, serves as the internal loading control. All data were from at least three independent experiments. In each independent experiment, N > 200 mitotic cells were counted for each sample. The error bars represent the SD. Statistical significance was calculated using unpaired t-tests and is reported as $P < 0.01$ **, $P < 0.001$ ***.

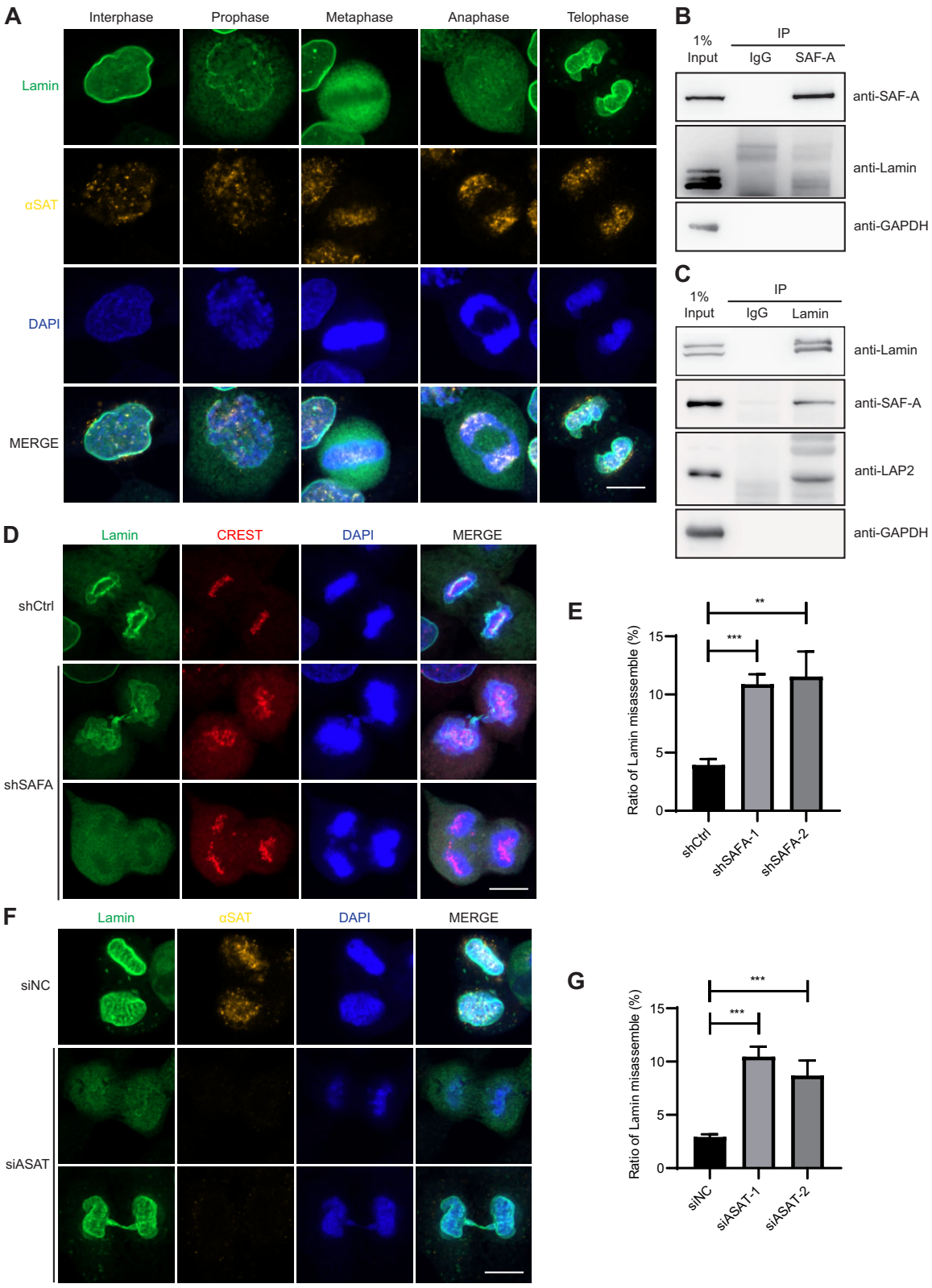

Figure 8. α-Satellite RNA regulates the reassembly of the nuclear lamina. (**A**) Representative images of α-satellite RNA smFISH and Lamin IF at different cell cycle stages. Scale bar, 10 μm. (**B**) IP with antibody against SAF-A in RPE1 cells with co-IP of Lamin. GAPDH serves as the negative control. (**C**) IP with antibody against Lamin in RPE1 cells with co-IP of SAF-A. LAP2 serves as the positive control, and GAPDH serves as the negative control. (**D**) Representative CREST and Lamin IF images show the misassembly of Lamin after the knockdown of SAF-A with shRNA. Scale bar, 10 μm. (**E**) Percentage of mitotic cells displaying misassembly of Lamin after shSAF-As transfection. (**F**) Representative α-satellite RNA smFISH and Lamin IF images show the abnormal location of Lamin after the knockdown of α-satellite RNAs with siASATs. Scale bar, 10 μm. (**G**) Percentage of mitotic cells displaying misassembly of Lamin after siASATs transfection. All data were from at least three independent experiments. In each independent experiment, N > 200 mitotic cells were counted for each sample. The error bars represent SD. Statistical significance was calculated using unpaired t-tests and is reported as $P < 0.01$ **, $P < 0.001$ ***.

These results demonstrate that α-satellite RNAs and SAF-A are crucial for the proper reassembly of the nuclear lamina upon mitotic exit.

Lamina-associated polypeptide 2 (LAP2) is a well-established interaction partner of the nuclear lamins and plays critical roles in mediating membrane-chromatin attachment and lamina assembly (Supplementary Fig. S11A) [27]. Consequently, we also assessed the impact of siASAT and shSAFA knockdown on LAP2. Although the immunoprecipitation assays did not reveal a direct interaction between SAF-A and LAP2 (Supplementary Fig. S11B), immunofluorescence analyses demonstrated that SAF-A or α-satellite RNA knockdown resulted in a significantly increased incidence of LAP2 misassembly in telophase cell (Supplementary Fig. S11C--F), which indicated that SAF-A and α-satellite RNA directly regulated nuclear lamins, and through this regulation, affected the recruitment of other nuclear membrane proteins such as LAP2. These findings further emphasize the important roles of α-satellite RNA and SAF-A in the proper assembly of the nuclear lamina at mitotic exit.

Overall, our results reveal that α-satellite RNAs are dynamically expressed in the mitotic cell cycle under the regulation of Aurora kinases and are transcribed bidirectionally to produce sense, antisense, and dsRNAs. α-Satellite RNAs physically interact with the SAF-A in a cell cycle-dependent manner. Unlike most other SAF-A binding RNAs, α-satellite RNAs remain associated with the centromeric chromatin throughout the mitotic cell cycle, whereas SAF-A undergoes dynamic dissociation and reassembly with the chromatin during mitosis (Fig. 9). Furthermore. the presence of α-satellite RNAs is required for the accurate dissociation and recruitment of SAF-A during mitosis, and together they play a notable role in the reconstruction of the nuclear lamina and the preservation of the genome integrity during mitosis.

Discussion

It has been reported that most RNAs that are stably associated with interphase chromosomes are repetitive in nature [64]. However, less is known about the RNA molecules that are associated with mitotic chromosomes. As the most abundant centromeric repeats, α-satellite originated transcripts are stably associated with chromosome centromere regions. Unlike most other caRNAs, which detach from the mitotic chromosomes, α-satellite RNAs appear to adhere tightly to the centromere regions. In this study, we demonstrated that these centromere chromatin-associated α-satellite RNAs are important for the recruitment of SAF-A at mitotic exit and participate in the maintenance of mitotic chromosome structure, reestablishment of the nuclear matrix, and the reassembly of nuclear lamina.

As demonstrated in this study, α-satellite RNAs are heterogeneous RNAs of sense, antisense, and dsRNAs with various lengths. Because of their high repetitiveness, it is challenging to precisely obtain the nucleotide sequences of α-satellite RNAs, which has hindered research on the functional roles of α-satellite RNAs to an extent. Current developments in genome sequencing and the completion of the human genome with all the repeat sequences have enabled the distinction of α-satellite RNAs from different genomic regions [2, 3]. In this study, we focused on the SAF-A, which can bind the α-satellite RNA sense, antisense, and dsRNA forms. The other α-satellite RNA interacting proteins identified in this study required further verification and investigation. It is possible that different α-satellite RNA forms or certain subsets of α-satellite RNA may possess some specific functions via distinct interactors, which needs to be addressed in future studies.

RNA pull-down and gel shift assay results revealed that α-satellite RNA specifically interacts with isoform a, but not with isoform b, of SAF-A (Fig. 4D and E). This finding is interesting given that the two isoforms differ by only 19 amino acid residues located within the IDR situated between the SAP and SPRY domains (Supplementary Fig. S5B). It is documented that SAF-A interacts with RNA via its C-terminal IDRs within the RGG domain [20]. The IDRs within SAF-A's AAA + domain have been suggested to facilitate its oligomerization with caRNAs, a process essential that is essential for maintaining the large-scale chromatin structure during interphase [21]. However, the function of the IDR located between the SAP and SPRY domains remains poorly understood. Our findings hint that these IDRs may contribute to the selective RNA binding of SAF-A. Further structural characterization of SAF-A is required to elucidate the molecular mechanisms underlying its selective RNA binding. Insights garnered from these studies would advance our understanding of SAF-A's diverse functions.

The transcription of α-satellite RNA is tightly regulated, and its proper expression is essential for centromere functionality as well as genome stability [12–14]. A key function of α-satellite RNA is its involvement in the assembly and maintenance of the kinetochore complex [5]. Previous studies have demonstrated that α-satellite RNA interacts with critical kinetochore proteins, including CENP-A and CENP-C, which are crucial for the accurate attachment of microtubules to chromosomes during prometaphase [9–11]. The presence of α-satellite RNA is necessary for the correct localization of these proteins, thereby ensuring precise chromosome segregation and preventing aneuploidy [10, 11]. Furthermore, α-satellite RNA plays a role in the regulation of centromere-nucleolus associations. These interactions are crucial for suppressing the expression of α-satellite transcripts during interphase, and their dysregulation can result in chromosomal instability [7]. Similarly, SAF-A is a multifunctional protein that performs various roles at different cell cycle stages [21, 32, 65]. In interphase cells, SAF-A plays a crucial role in preserving the structural integrity of chromatin as well as regulating gene expression. It interacts with caRNAs to form a dynamic chromatin mesh that arranges large-scale chromosomal structures and maintains genome stability [21]. Conversely, in mitotic cells, SAF-A is implicated in the redistribution of RNAs away from chromosomes, which is a process that is essential for ensuring the fidelity of chromosome segregation, thereby emphasizing SAF-A's involvement in chromosomal remodeling during cell division [32]. In addition, it has been reported that SAF-A undergoes phosphorylation at serine 59 during cell division, a modification that is proposed to be vital for accurate chromosome alignment and segregation, as mutations at this site result in mitotic anomalies [65]. Both α-satellite RNA and SAF-A appear to undergo functional transformations throughout the mitotic cell cycle. In this study, we demonstrated that the transient disassociation and re-association of α-satellite RNA and SAF-A are critical for maintaining genomic integrity during mitosis and for the reassembly of the nuclear lamina upon mitotic exit.

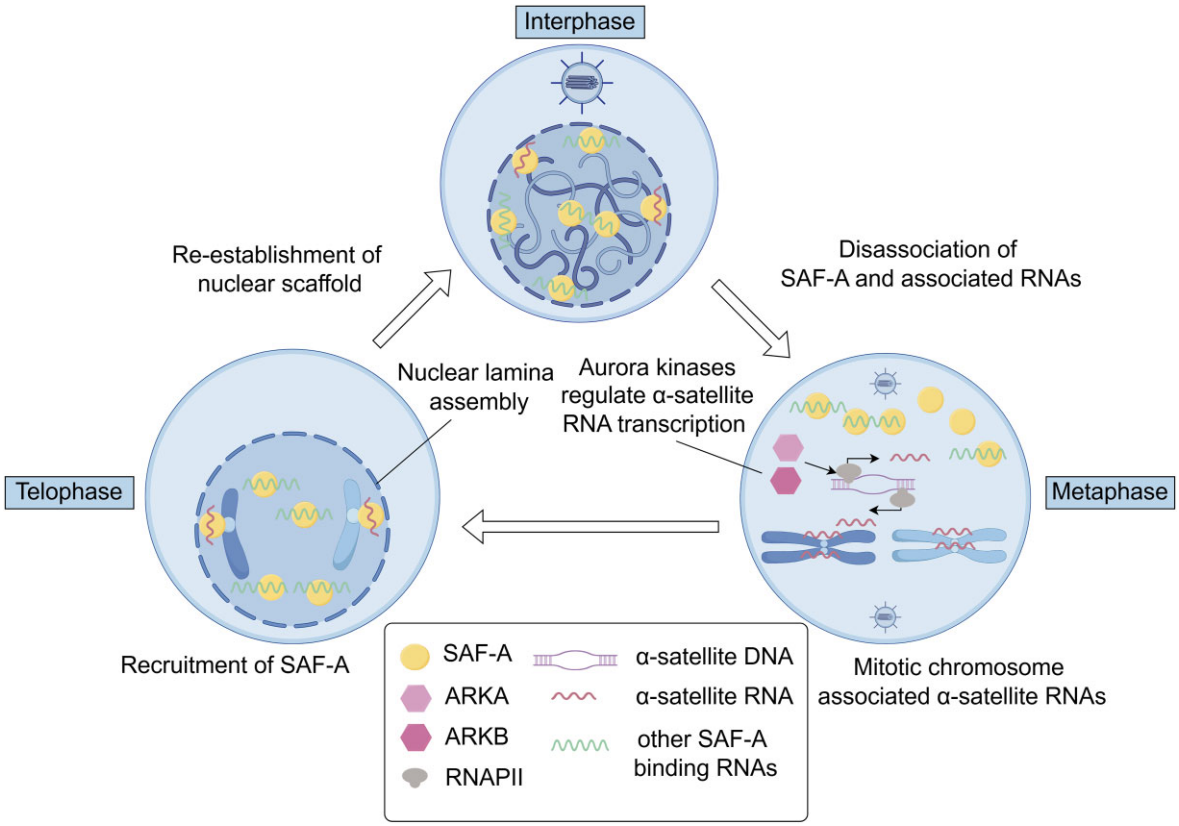

Figure 9. A working model of α-satellite RNAs and SAF-A during mitosis. Both α-satellite RNA and its interacting partner SAF-A are chromatin-associated in interphase cells. Most caRNAs and SAF-A are excluded from the mitotic chromosomes to allow proper chromosome condensation. Whereas, α-satellite RNAs are tightly associated with the centromere throughout the cell cycle. The cell cycle-dependent expression of α-satellite RNA is regulated by Aurora kinases. α-Satellite RNA facilitates the re-establishment of SAF-A in telophase and together aid in regulating the chromatin and nuclear lamina at mitotic exit.

During the cell cycle, chromatin undergoes considerable structural transitions, which are essential for gene expression regulation and the maintenance of genomic stability. These transitions are tightly regulated and include a complex interplay of chromatin-associated proteins and RNAs. The exclusion of caRNAs from mitotic chromosomes is a critical aspect of chromatin dynamics during cell division [32, 66]. This study identified α-satellite RNA as a caRNA that remains associated with chromosomes during mitosis (Fig. 3). SAF-A is recognized as a key protein in maintaining chromatin structure during interphase [21]; however, we discover that during mitosis SAF-A is released from the chromatin, which may be a part of the broader chromatin structure reorganization. Our study demonstrates that SAF-A is released from chromatin in cells transitioning from metaphase to anaphase (Fig. 5A). Furthermore, SAF-A CUT&Tag and RIP analyses reveal a modest yet significant reduction in chromatin-associated SAF-A during mitosis, both genome-wide and at the centromere regions (Fig. 5B–E). The observed variation in the extent of SAF-A exclusion from chromatin may be attributed to the fact that not all synchronized cells precisely align within the metaphase-to-anaphase of the cell cycle, suggesting that SAF-A exclusion and recruitment occur within a very brief time frame. The failure to recruit SAF-A immediately following this period impairs nuclear lamina reassembly at the mitotic exit (Fig. 8).

Repetitive RNAs have been reported to be innately stable [64]. In particular, a recent study showed that some RNAs derived from major and minor satellites can be retained in mouse brain cells for years and help to maintain the centromeric heterochromatin [67]. Our study demonstrates that, through its association with centromeric chromatin, α-satellite RNAs may help re-establish the chromatin structure in the next cell cycle. α-Satellite RNAs are degraded by endogenous RNA interference [11], and we show here that α-satellite RNAs are being actively transcribed during mitosis and promoted by Aurora kinases. A delicate balance of α-satellite RNA levels is required to maintain genome integrity during the series of chromatin structural changes in mitosis. Further studies are required to examine whether α-satellite dsRNAs can be processed into endogenous siRNAs, which can then regulate the levels of sense and antisense α-satellite transcripts through the endogenous RNA interference pathway. How the production and eradication of α-satellite RNAs are coordinated to ensure the proper levels and functions of α-satellite RNAs also needs further study.

Other than in human cells, centromeric satellite RNAs have been identified in almost all eukaryotes, such as in mice, flies, nematodes, and yeasts. Despite the large differences in their nucleotide sequences, these satellite RNAs appear to perform some common functions [8, 68]. Here, we revealed that the major satellite RNAs in mouse cells are expressed in a

cell cycle-dependent manner. Furthermore, the interaction between the centromeric satellite RNA and SAF-A is also observed with mouse major satellite RNA, but not with minor satellite RNA, suggesting a partially conserved function of the centromeric satellite RNA/SAF-A complex in regulating chromatin and the nuclear matrix during mitosis.

Acknowledgements

We thank Dr. Xiaolin Wang and Dr. Chuan Huang for their helpful and constructive comments that improve this study substantially. We thank Dr. Chao Bi from the Core Facilities, Zhejiang University School of Medicine for her technical support. Model figures were created by FigDraw (www.figdraw.com) with permission..

Author contributions: B.R. and G.S. conceived and designed this project. B.R., Y.Z., Y.Y., S.C., Y.L., and M.Y. performed experiments and analyses. B.R., X.W., and E.C. wrote the manuscript and provided major funding and resources. All authors have discussed the results and made comments on the manuscript. All authors approved the final manuscript.

Supplementary data

Supplementary data is available at NAR online.

Conflict of interest

The authors declare no conflict of interest.

Funding

This study was supported by the National Natural Science Foundation of China [32000437 and U23A20164]; the Key R&D Program of Zhejiang [2022C03086]; the Medical Science and Technology Project of Zhejiang Province [2023RC188]; and the Natural Science Foundation of Anhui Province [2408085QC090]. Funding to pay the Open Access publication charges for this article was provided by the National Natural Science Foundation of China [32000437 and U23A20164]; the Key R&D Program of Zhejiang [2022C03086]; the Medical Science and Technology Project of Zhejiang Province [2023RC188]; and the Natural Science Foundation of Anhui Province [2408085QC090].

Data availability

The ChIRP-seq, CUT&Tag, and EU-RNA-seq data are deposited in GEO (https://www.ncbi.nlm.nih.gov/geo/) and can be assessed with GSE270307, GSE286152, and GSE286151, respectively. Other publicly available sequencing datasets used in this study can be accessed with GSM6429694 and GSM3852804.

References

1. McKinley KL, Cheeseman IM. The molecular basis for centromere identity and function. *Nat Rev Mol Cell Bio* 2016;**17**:16–29.
2. Altemose N, Logsdon GA, Bzikadze AV *et al.* Complete genomic and epigenetic maps of human centromeres. *Science* 2022;**376**:eabl4178.
3. Hoyt SJ, Storer JM, Hartley GA *et al.* From telomere to telomere: the transcriptional and epigenetic state of human repeat elements. *Science* 2022;**376**:eabk3112.
4. Schueler MG, Higgins AW, Rudd MK *et al.* Genomic and genetic definition of a functional human centromere. *Science* 2001;**294**:109–15.
5. Wong LH, Brettingham-Moore KH, Chan L *et al.* Centromere RNA is a key component for the assembly of nucleoproteins at the nucleolus and centromere. *Genome Res* 2007;**17**:1146–60.
6. Chan FL, Marshall OJ, Saffery R *et al.* Active transcription and essential role of RNA polymerase II at the centromere during mitosis. *P Natl Acad Sci Usa* 2012;**109**:1979–84.
7. Bury L, Moodie B, Ly J *et al.* Alpha-satellite RNA transcripts are repressed by centromere-nucleolus associations. *eLife* 2020;**9**:e59770.
8. Arunkumar G, Melters DP. Centromeric transcription: a conserved Swiss-Army knife. *Genes (Basel)* 2020;**11**:911.
9. Quenet D, Dalal Y. A long non-coding RNA is required for targeting centromeric protein A to the human centromere. *eLife* 2014;**3**:e03254.
10. McNulty SM, Sullivan LL, Sullivan BA. Human centromeres produce chromosome-specific and array-specific alpha satellite transcripts that are complexed with CENP-A and CENP-C. *Dev Cell* 2017;**42**:226–240.e6. https://doi.org/10.1016/j.devcel.2017.07.001
11. Huang C, Wang X, Liu X *et al.* RNAi pathway participates in chromosome segregation in mammalian cells. *Cell Discov* 2015;**1**:15029. https://doi.org/10.1038/celldisc.2015.29
12. Eymery A, Horard B, El AM *et al.* A transcriptomic analysis of human centromeric and pericentric sequences in normal and tumor cells. *Nucleic Acids Res* 2009;**37**:6340–54. https://doi.org/10.1093/nar/gkp639
13. Ting DT, Lipson D, Paul S *et al.* Aberrant overexpression of satellite repeats in pancreatic and other epithelial cancers. *Science* 2011;**331**:593–6. https://doi.org/10.1126/science.1200801
14. Zhu Q, Pao GM, Huynh AM *et al.* BRCA1 tumour suppression occurs via heterochromatin-mediated silencing. *Nature* 2011;**477**:179–84. https://doi.org/10.1038/nature10371
15. Chan D, Moralli D, Khoja S *et al.* Noncoding centromeric RNA expression impairs chromosome stability in Human and murine stem cells. *Dis Markers* 2017;**2017**:1–8. https://doi.org/10.1155/2017/7506976
16. Talbert PB, Henikoff S. Transcribing centromeres: noncoding RNAs and kinetochore assembly. *Trends Genet* 2018;**34**:587–99. https://doi.org/10.1016/j.tig.2018.05.001
17. Ninomiya K, Yamazaki T, Hirose T. Satellite RNAs: emerging players in subnuclear architecture and gene regulation. *EMBO J* 2023;**42**:e114331. https://doi.org/10.15252/embj.2023114331
18. Johnson WL, Yewdell WT, Bell JC *et al.* RNA-dependent stabilization of SUV39H1 at constitutive heterochromatin. *eLife* 2017;**6**:e25299. https://doi.org/10.7554/eLife.25299
19. Romig H, Fackelmayer FO, Renz A *et al.* Characterization of SAF-A, a novel nuclear DNA binding protein from HeLa cells with high affinity for nuclear matrix/scaffold attachment DNA elements. *EMBO J* 1992;**11**:3431–40. https://doi.org/10.1002/j.1460-2075.1992.tb05422.x
20. Kiledjian M, Dreyfuss G. Primary structure and binding activity of the hnRNP U protein: binding RNA through RGG box. *EMBO J* 1992;**11**:2655–64. https://doi.org/10.1002/j.1460-2075.1992.tb05331.x
21. Nozawa RS, Boteva L, Soares DC *et al.* SAF-A regulates interphase chromosome structure through oligomerization with chromatin-associated RNAs. *Cell* 2017;**169**:1214–27. https://doi.org/10.1016/j.cell.2017.05.029
22. Fan H, Lv P, Huo X *et al.* The nuclear matrix protein HNRNPU maintains 3D genome architecture globally in mouse hepatocytes. *Genome Res* 2018;**28**:192–202. https://doi.org/10.1101/gr.224576.117
23. Creamer KM, Kolpa HJ, Lawrence JB. Nascent RNA scaffolds contribute to chromosome territory architecture and counter chromatin compaction. *Mol Cell* 2021;**81**:3509–25. https://doi.org/10.1016/j.molcel.2021.07.004

24. Xiao R, Tang P, Yang B *et al.* Nuclear matrix factor hnRNP U/SAF-A exerts a global control of alternative splicing by regulating U2 snRNP maturation. *Mol Cell* 2012;**45**:656–68. https://doi.org/10.1016/j.molcel.2012.01.009
25. Guelen L, Pagie L, Brasset E *et al.* Domain organization of human chromosomes revealed by mapping of nuclear lamina interactions. *Nature* 2008;**453**:948–51. https://doi.org/10.1038/nature06947
26. Falk M, Feodorova Y, Naumova N *et al.* Heterochromatin drives compartmentalization of inverted and conventional nuclei. *Nature* 2019;**570**:395–9. https://doi.org/10.1038/s41586-019-1275-3
27. Burke B, Stewart CL. The nuclear lamins: flexibility in function. *Nat Rev Mol Cell Biol* 2013;**14**:13–24. https://doi.org/10.1038/nrm3488
28. Skalska L, Begley V, Beltran M *et al.* Nascent RNA antagonizes the interaction of a set of regulatory proteins with chromatin. *Mol Cell* 2021;**81**:2944–59. https://doi.org/10.1016/j.molcel.2021.05.026
29. Marenda M, Lazarova E, van de Linde S *et al.* Parameter-free molecular super-structures quantification in single-molecule localization microscopy. *J Cell Biol* 2021;**220**:e202010003. https://doi.org/10.1083/jcb.202010003
30. Huelga SC, Vu AQ, Arnold JD *et al.* Integrative genome-wide analysis reveals cooperative regulation of alternative splicing by hnRNP proteins. *Cell Rep* 2012;**1**:167–78. https://doi.org/10.1016/j.celrep.2012.02.001
31. Van Nostrand EL, Freese P, Pratt GA *et al.* A large-scale binding and functional map of human RNA-binding proteins. *Nature* 2020;**583**:711–9. https://doi.org/10.1038/s41586-020-2077-3
32. Sharp JA, Perea-Resa C, Wang W *et al.* Cell division requires RNA eviction from condensing chromosomes. *J Cell Biol* 2020;**219**:e201910148. https://doi.org/10.1083/jcb.201910148
33. Choi HM, Beck VA, Pierce NA. Next-generation in situ hybridization chain reaction: higher gain, lower cost, greater durability. *ACS Nano* 2014;**8**:4284–94. https://doi.org/10.1021/nn405717p
34. Choi HM, Chang JY, Trinh LA *et al.* Programmable in situ amplification for multiplexed imaging of mRNA expression. *Nat Biotechnol* 2010;**28**:1208–12. https://doi.org/10.1038/nbt.1692
35. Chu C, Quinn J, Chang HY. Chromatin isolation by RNA purification (ChIRP). *Jove (J Vis Exp)* 2012;**61**:e3912.
36. Chu C, Qu K, Zhong FL *et al.* Genomic maps of long noncoding RNA occupancy reveal principles of RNA-chromatin interactions. *Mol Cell* 2011;**44**:667–78. https://doi.org/10.1016/j.molcel.2011.08.027
37. Friskes A, Koob L, Krenning L *et al.* Double-strand break toxicity is chromatin context independent. *Nucleic Acids Res* 2022;**50**:9930–47. https://doi.org/10.1093/nar/gkac758
38. Langmead B, Salzberg SL. Fast gapped-read alignment with Bowtie 2. *Nat Methods* 2012;**9**:357–9. https://doi.org/10.1038/nmeth.1923
39. Zhang Y, Liu T, Meyer CA *et al.* Model-based analysis of ChIP-Seq (MACS). *Genome Biol* 2008;**9**:R137. https://doi.org/10.1186/gb-2008-9-9-r137
40. Krzywinski M, Schein J, Birol I *et al.* Circos: an information aesthetic for comparative genomics. *Genome Res* 2009;**19**:1639–45. https://doi.org/10.1101/gr.092759.109
41. Gu Z, Gu L, Eils R *et al.* circlize implements and enhances circular visualization in R. *Bioinformatics* 2014;**30**:2811–2. https://doi.org/10.1093/bioinformatics/btu393
42. Li J, Wang X, Shi L *et al.* A mammalian conserved circular RNA CircLARP1B regulates hepatocellular carcinoma metastasis and lipid metabolism. *Adv Sci* 2024;**11**:e2305902. https://doi.org/10.1002/advs.202305902
43. Brenner S, Pepper D, Berns MW *et al.* Kinetochore structure, duplication, and distribution in mammalian cells: analysis by human autoantibodies from scleroderma patients. *J Cell Biol* 1981;**91**:95–102. https://doi.org/10.1083/jcb.91.1.95
44. Zheng F, Yue C, Li G *et al.* Nuclear AURKA acquires kinase-independent transactivating function to enhance breast cancer stem cell phenotype. *Nat Commun* 2016;**7**:10180. https://doi.org/10.1038/ncomms10180
45. Vukusic K, Ponjavic I, Buda R *et al.* Microtubule-sliding modules based on kinesins EG5 and PRC1-dependent KIF4A drive human spindle elongation. *Dev Cell* 2021;**56**:1253–1267.e10. https://doi.org/10.1016/j.devcel.2021.04.005
46. Huang KC, Chiang SF, Chang HY *et al.* Colorectal cancer-specific IFNbeta delivery overcomes dysfunctional dsRNA-mediated type I interferon signaling to increase the abscopal effect of radiotherapy. *J Immunother Cancer* 2024;**12**:e008515. https://doi.org/10.1136/jitc-2023-008515
47. Yuan H, Wu X, Wu Q *et al.* Lysine catabolism reprograms tumour immunity through histone crotonylation. *Nature* 2023;**617**:818–26. https://doi.org/10.1038/s41586-023-06061-0
48. Eot-Houllier G, Magnaghi-Jaulin L, Fulcrand G *et al.* Aurora A-dependent CENP-A phosphorylation at inner centromeres protects bioriented chromosomes against cohesion fatigue. *Nat Commun* 2018;**9**:1888. https://doi.org/10.1038/s41467-018-04089-9
49. Liang C, Zhang Z, Chen Q *et al.* Centromere-localized Aurora B kinase is required for the fidelity of chromosome segregation. *J Cell Biol* 2020;**219**:e201907092. https://doi.org/10.1083/jcb.201907092
50. Littlepage LE, Wu H, Andresson T *et al.* Identification of phosphorylated residues that affect the activity of the mitotic kinase aurora-A. *Proc Natl Acad Sci USA* 2002;**99**:15440–5. https://doi.org/10.1073/pnas.202606599
51. Yasui Y, Urano T, Kawajiri A *et al.* Autophosphorylation of a newly identified site of aurora-B is indispensable for cytokinesis. *J Biol Chem* 2004;**279**:12997–3003. https://doi.org/10.1074/jbc.M311128200
52. Van Brocklyn JR, Wojton J, Meisen WH *et al.* Aurora-A inhibition offers a novel therapy effective against intracranial glioblastoma. *Cancer Res* 2014;**74**:5364–70. https://doi.org/10.1158/0008-5472.CAN-14-0386
53. Liu M, Ju X, Zou J *et al.* Recent researches for dual Aurora target inhibitors in antitumor field. *Eur J Med Chem* 2020;**203**:112498. https://doi.org/10.1016/j.ejmech.2020.112498
54. Asteriti IA, Giubettini M, Lavia P *et al.* Aurora-A inactivation causes mitotic spindle pole fragmentation by unbalancing microtubule-generated forces. *Mol Cancer* 2011;**10**:131. https://doi.org/10.1186/1476-4598-10-131
55. Santaguida S, Vernieri C, Villa F *et al.* Evidence that Aurora B is implicated in spindle checkpoint signalling independently of error correction. *Embo J* 2011;**30**:1508–19. https://doi.org/10.1038/emboj.2011.70
56. Kim SR, Kim KB, Chae YC *et al.* H3S10 phosphorylation-mediated transcriptional regulation by Aurora kinase A. *Biochem Biophys Res Commun* 2016;**469**:22–8. https://doi.org/10.1016/j.bbrc.2015.11.063
57. Li Y, Kao GD, Garcia BA *et al.* A novel histone deacetylase pathway regulates mitosis by modulating Aurora B kinase activity. *Genes Dev* 2006;**20**:2566–79. https://doi.org/10.1101/gad.1455006
58. Milletti G, Colicchia V, Cecconi F. Cyclers' kinases in cell division: from molecules to cancer therapy. *Cell Death Differ* 2023;**30**:2035–52. https://doi.org/10.1038/s41418-023-01196-z
59. Dumont M, Gamba R, Gestraud P *et al.* Human chromosome-specific aneuploidy is influenced by DNA-dependent centromeric features. *EMBO J* 2020;**39**:e102924. https://doi.org/10.15252/embj.2019102924
60. Fackelmayer FO, Richter A. Purification of two isoforms of hnRNP-U and characterization of their nucleic acid binding activity. *Biochemistry* 1994;**33**:10416–22. https://doi.org/10.1021/bi00200a024
61. Jumper J, Evans R, Pritzel A *et al.* Highly accurate protein structure prediction with AlphaFold. *Nature* 2021;**596**:583–9. https://doi.org/10.1038/s41586-021-03819-2

62. Linding R, Jensen LJ, Diella F *et al.* Protein disorder prediction: implications for structural proteomics. *Structure* 2003;**11**:1453–9. https://doi.org/10.1016/j.str.2003.10.002
63. Foisner R, Gerace L. Integral membrane proteins of the nuclear envelope interact with lamins and chromosomes, and binding is modulated by mitotic phosphorylation. *Cell* 1993;**73**:1267–79. https://doi.org/10.1016/0092-8674(93)90355-T
64. Hall LL, Carone DM, Gomez AV *et al.* Stable C0T-1 repeat RNA is abundant and is associated with euchromatic interphase chromosomes. *Cell* 2014;**156**:907–19. https://doi.org/10.1016/j.cell.2014.01.042
65. Douglas P, Ye R, Morrice N *et al.* Phosphorylation of SAF-A/hnRNP-U serine 59 by polo-like kinase 1 is required for mitosis. *Mol Cell Biol* 2015;**35**:2699–713. https://doi.org/10.1128/MCB.01312-14
66. Shen W, Zhang Y, Shi M *et al.* Profiling and characterization of constitutive chromatin-enriched RNAs. iScience 2022;**25**:105349. https://doi.org/10.1016/j.isci.2022.105349
67. Zocher S, McCloskey A, Karasinsky A *et al.* Lifelong persistence of nuclear RNAs in the mouse brain. *Science* 2024;**384**:53–9. https://doi.org/10.1126/science.adf3481
68. Chan FL, Wong LH. Transcription in the maintenance of centromere chromatin identity. *Nucleic Acids Res* 2012;**40**:11178–88. https://doi.org/10.1093/nar/gks921

Received: July 6, 2024. **Revised:** March 21, 2025. **Editorial Decision:** March 24, 2025. **Accepted:** March 28, 2025